JOURNAL OF GEOPHYSICAL RESEARCH, VOL. 102, NO. B5, PAGES 9859-9886, MAY 10, 1997

Evolution of the stress field in southern California and triggering of moderate-size earthquakes: A 200-year perspective

Jishu Deng and Lynn R. Sykes

Lamont-Doherty Earth Observatory, Columbia University, Palisades, New York
Department of Earth and Environmental Sciences, Columbia University, New York

Abstract. Changes in stress in southern California are modeled from 1812 to 2025 using as input (1) stress drops associated with six large ($7.0 \leq M < 7.5$) to great ($M \geq 7.5$) earthquakes through 1995 and (2) stress buildup associated with major faults with slip rates ≥ 3 mm/yr as constrained by geodetic, paleoseismic, and seismic measurements. Evolution of stress and the triggering of moderate to large earthquakes are treated in a tensorial rather than a scalar manner. We present snapshots of the cumulative Coulomb failure function (ΔCFF) as a function of time for faults of various strike, dip, and rake throughout southern California. We take ΔCFF to be zero everywhere just prior to the great shock of 1812. We find that about 95% of those well-located $M \geq 6$ earthquakes whose mechanisms involve either strike-slip or reverse faulting are consistent with the Coulomb stress evolutionary model; that is, they occurred in areas of positive ΔCFF. The interaction between slow-moving faults and stresses generated by faster-moving faults significantly advanced the occurrence of the 1933 Long Beach and 1992 Landers events in their earthquake cycles. Coulomb stresses near major thrust faults of the western and central Transverse Ranges have been accumulating for a long time. Future great earthquakes along the San Andreas fault, especially if the San Bernardino and Coachella Valley segments rupture together, can trigger moderate to large earthquakes in the Transverse Ranges, as appears to have happened in the Santa Barbara earthquake that occurred 13 days after the great San Andreas shock of 1812. Maps of current ΔCFF provide additional guides to long-term earthquake prediction.

Introduction

The state of stress and its variation with time are two of the most fundamental physical parameters controlling the earthquake process. An earthquake occurs when the stress exceeds the strength of the corresponding fault. Earthquakes in a sequence generally are not independent [*Scholz*, 1990]. Each is affected by both tectonic loading and stress changes caused by prior events, especially by either great earthquakes or other shocks that occur nearby.

Large earthquakes can affect the rates of occurrence of nearby microearthquakes. Changes in stress caused by the 1989 Loma Prieta earthquake, for example, are correlated with the rates of occurrence of small earthquakes on central California faults [*Reasenberg and Simpson*, 1992; *Simpson and Reasenberg*, 1994]. Similarly, moderate to large earthquakes in central and northern California are believed to occur only after the stresses have recovered from the stress release associated with previous great earthquakes. *Simpson and Reasenberg* [1994] computed the accumulated changes in stress for segments of the Hayward and Calaveras faults in central California since the 1906 San Francisco (M_w=7.8) [*Wald et al.*, 1993] earthquake. Their result for segments of the Calaveras fault indicates that $M \geq 5$ earthquakes started to reoccur after stresses had recovered from the shadow zone created by the occurrence of the 1906 event. In their study on evolution of the stress field in the San Francisco Bay region for the period between 1850 and 1993, *Jaumé and Sykes* [1996] also found that moderate-size earthquakes occurred in regions that were located either outside of or had recovered via strain accumulation from the stress shadows created by past large and great earthquakes.

The configuration of the plate boundary in southern California (Figure 1), the region of interest to this paper, is much more complicated than that in the bay area. Stress changes in southern California have often been investigated on an earthquake-by-earthquake basis. Large earthquakes, such as the 1812 Wrightwood, 1857 great Fort Tejon (M_w = 7.9), 1992 Landers (M_w = 7.3), and 1994 Northridge (M_w = 6.7) earthquakes, have all been shown to advance the time of occurrence, i.e., to trigger subsequent, moderate-size events [*Harris and Simpson*, 1992; *Jaumé and Sykes*, 1992; *Stein et al.*, 1992; *King et al.*, 1994; *Stein et al.*, 1994; *Simpson and Reasenberg*, 1994; *Harris et al.*, 1995; *Deng and Sykes*, 1996]. Southern California, however, is one of a few regions in the world where extensive earthquake-related monitoring studies have been underway for many years. Much progress has been made in the past decade in collecting a variety of data bearing upon the earthquake process and the state of stress in southern California. These data include geodetic measurements, focal mechanism solutions of earthquakes, long-term rates of fault slip, fault geometries, paleoseismic determinations of displacement in prehistoric events, and better modeling of historic shocks. While the direct measurement of stress changes is very difficult, it is now possible to pull together stress-related data to infer the time-dependent cumulative stress

Paper number 96JB03897.
0148-0227/97/96JB-03897$09.00

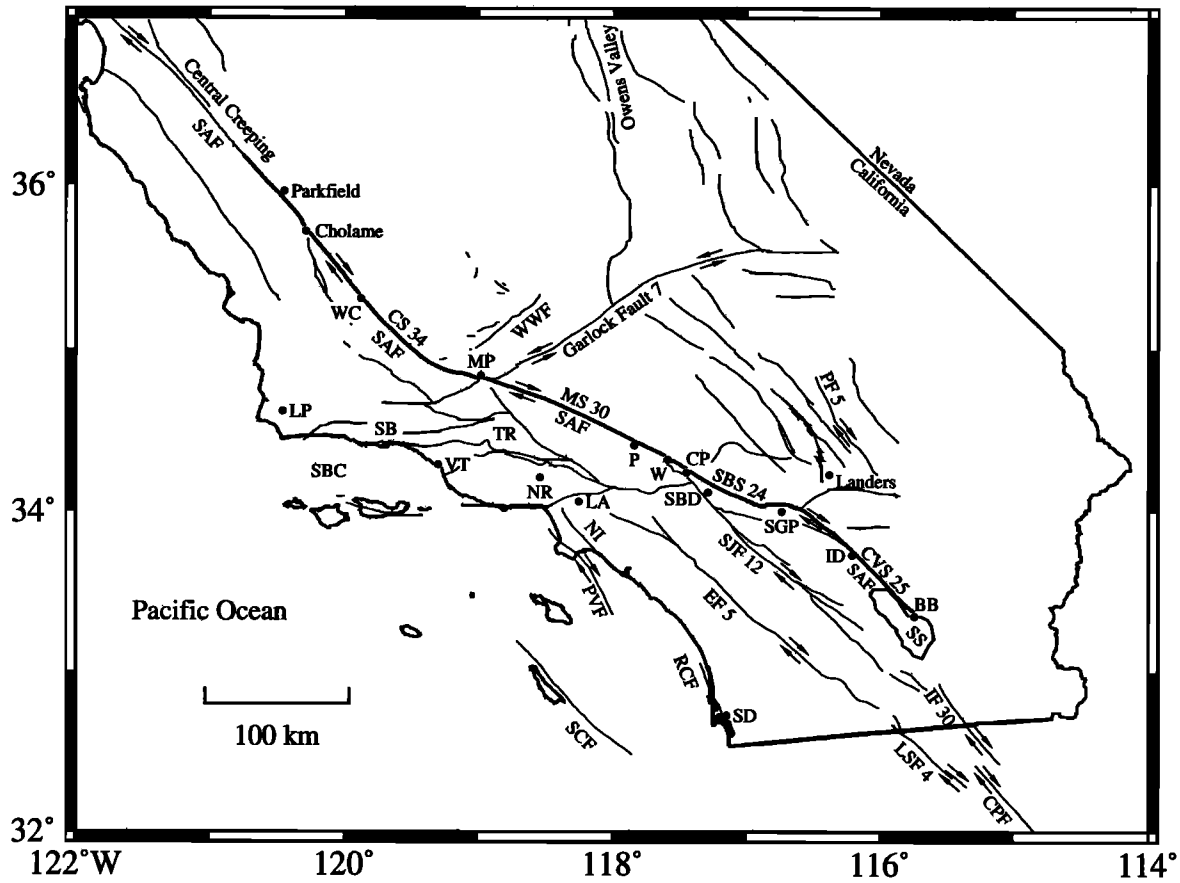

Figure 1. Major place names, active faults, and fault segments in southern California. Long-term slip rates of selected segments of San Andreas (SAF) and other major faults are shown in millimeters per year [*Petersen and Wesnousky,* 1994; *Working Group,* 1995]. Segments of San Andreas fault are CS, Carrizo; CVS, Coachella Valley; MS, Mojave; SBS, San Bernardino. Other faults are CPF, Cerro Prieto; EF, Elsinore; IF, Imperial; LSF, Laguna Salada; NI, Newport-Inglewood; PF, Pisgah; PVF, Palos Verdes; RCF, Rose Canyon; SCF, San Clemente; SJF, San Jacinto; WWF, White Wolf. Other abbreviations are BB, Bombay Beach; CP, Cajon Pass; ID, Indio; LA, Los Angeles; LP, Lompoc; MP, Mill Potrero; NR, Northridge; P, Pallet Creek; SB, Santa Barbara; SBC, Santa Barbara Channel; SBD, San Bernardino; SD, San Diego; SGP, San Gorgonio Pass; SS, Salton Sea; TR, Transverse Ranges, which represents a much broader region than actually shown; VT, Ventura; W, Wrightwood; and WC, Wallace Creek. Arrows denote sense of long-term relative motion across faults. See Figure 3 for well-located recent small earthquakes along southern San Andreas fault (thick line).

tensor for earthquake hazard analyses and for long-term earthquake prediction. The newly available information permits the changes in the stress tensor to be mapped both in space and time in a manner not previously possible.

The goal of this paper is to understand the history of cumulative changes in stress throughout the fault network of southern California from 1812 to the present using a simple dislocation model in an elastic half-space. Since the geometry of active faults in southern California varies considerably in strike, dip, and rake, the changes in stress accumulation and the effects of a large to great shock along a given nearby fault (field point) must be treated in a tensorial manner rather than either dealing with a single component of the stress tensor or treating earthquake generation as a scalar. For southern California, this has been done for coseismic stress changes associated with one or more earthquakes [e.g., *Harris and Simpson,* 1993; *Stein et al.,* 1994]. However, stress effects of tectonic loading were not included in previous studies of that region. We take into account both coseismic stress changes associated with the occurrence of large to great earthquakes and stress accumulation associated with tectonic loading on major faults in southern California to calculate the history of stress for several typical styles of faulting where moderate- to large-size earthquakes have occurred since 1812. The history of cumulative changes in stress can be compared with the catalog of seismicity in the context of individual strike, dip, and rake to detect triggering, i.e., to ascertain if the site of an earthquake had been moved closer to or farther away from failure prior to its occurrence. The present state of stress also has profound implications on the likelihood of future great earthquakes.

Model Description

We consider stress to be a tensor quantity that varies with time and space. A tensor description is necessary, because southern California is a transpressional environment, where both horizontal and vertical loading is important. In this paper, stress is assumed to be transmitted elastically, with the Earth approximated as an homogeneous half-space.

Cumulative changes in stress are assumed to arise from the following two sources: tectonic loading generated by plate motions and coseismic displacements on faults associated with

earthquakes. Interseismic stress accumulation between large to great events is modeled by introducing "virtual negative displacements" along major faults in the entire southern California region using the best available information of their long-term slip rates. Hence stress builds up along faults during the time intervals between earthquakes. Similar approaches were used by *Savage and Burford* [1973], *Savage* [1983], and *Matsuura et al.* [1986]. Deep dislocation modeling gives nearly identical interseismic loading results to our virtual displacement method. Figures 2a and 2b illustrate our loading models for strike-slip and thrust faults, respectively. The interseismic deformation associated with a strike-slip fault is taken to be equivalent to the effect caused by a steady, relative motion between the two blocks below the maximum locking or seismogenic depth h in an elastic half-space and stress accumulation from depths $0 \le z \le h$. This loading process can be decomposed into a rigid offset throughout the whole half-space of the materials across the fault and a virtual dislocation of opposite sign extending from the free surface ($z=0$) to the seismogenic depth. The latter is approximated in our paper by the depth of the deepest small earthquakes that have recently occurred along the fault segments and are well located (Figure 3). Both the amount of offset and dislocation grow with time but cancel, so no slip occurs on the fault. Stress on and near the fault also changes with time, but no stress accumulation is associated with the rigid motion. Thus all interseismic stress accumulation is associated with the deformation caused by the time-dependent virtual displacement on major faults extending from the free surface to the seismogenic depth. The stress buildup is released wholly or in part during the next large to great earthquake, with positive real displacements on given fault segments.

Changes in stress associated with large to great earthquakes are calculated by putting certain coseismic displacements on ruptured fault segments in the elastic half-space and adding the changes in the components of the stress tensor together as they occur in time. Six large to great earthquakes of $7.0 \le M_w \le 8.1$ from 1812 to 1992 and one candidate future earthquake of M_w =

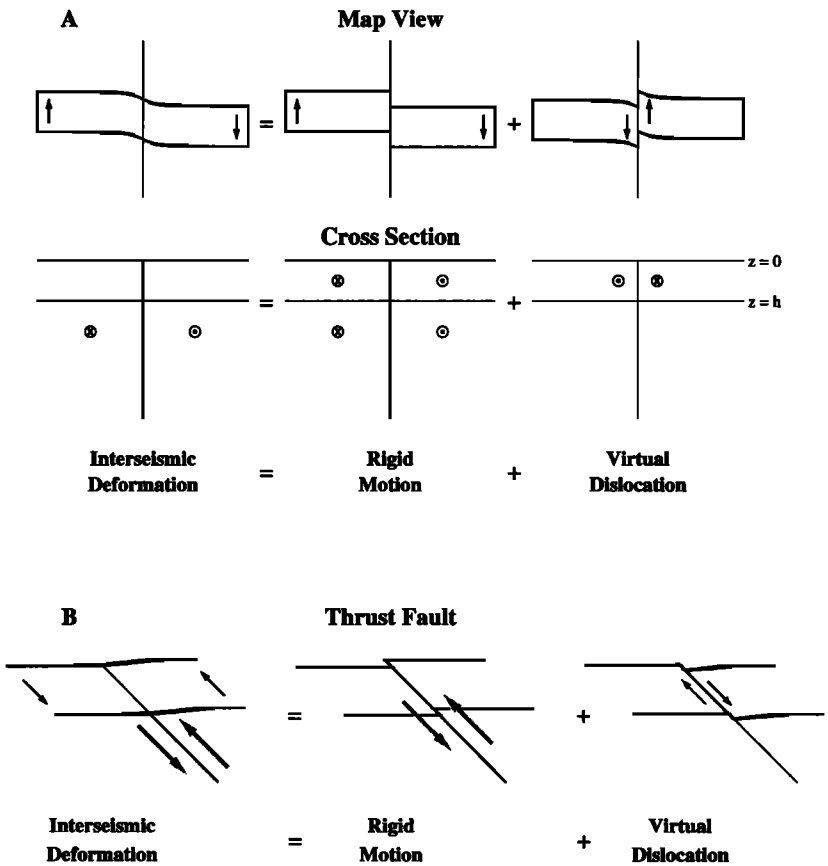

Figure 2. (a) Interseismic deformation at surface of Earth in the vicinity of a right-lateral strike-slip fault (thin lines in map views). (Left) Interseismic deformation, which can be modeled by locking the upper part of the fault ($0 \le z \le h$) and letting its lower part (thick line in cross section, $h < z < \infty$) move continuously in an aseismic manner. Deformation can be decomposed into (center) a rigid relative motion of the two quarter spaces along solid line in cross section ($0 \le z < \infty$) without any strain accumulation and a (right) deformation field generated by a virtual left-lateral dislocation along the same fault from $0 \le z \le h$. Since there is no stress change associated with the rigid motion (center), changes in stress can be modeled by the virtual dislocation shown at right. Accumulated stresses are released partly or totally in future earthquakes. In cross sections a circled cross indicates motion into page; a circled dot indicates motion out of page. (b) Interseismic deformation associated with a thrust fault. Deformation can be modeled by locking the upper part of the fault from the surface to seismogenic depth h as in Figure 2a and allowing it to slip continuously in an aseismic manner at greater depth. That deformation can be decomposed into a rigid motion of the right quarter space over the left along the thrust fault (center) and a virtual normal faulting dislocation (right) along that part of the fault extending from the surface to the seismogenic depth h. Stress accumulation is equal to that generated by the virtual normal fault.

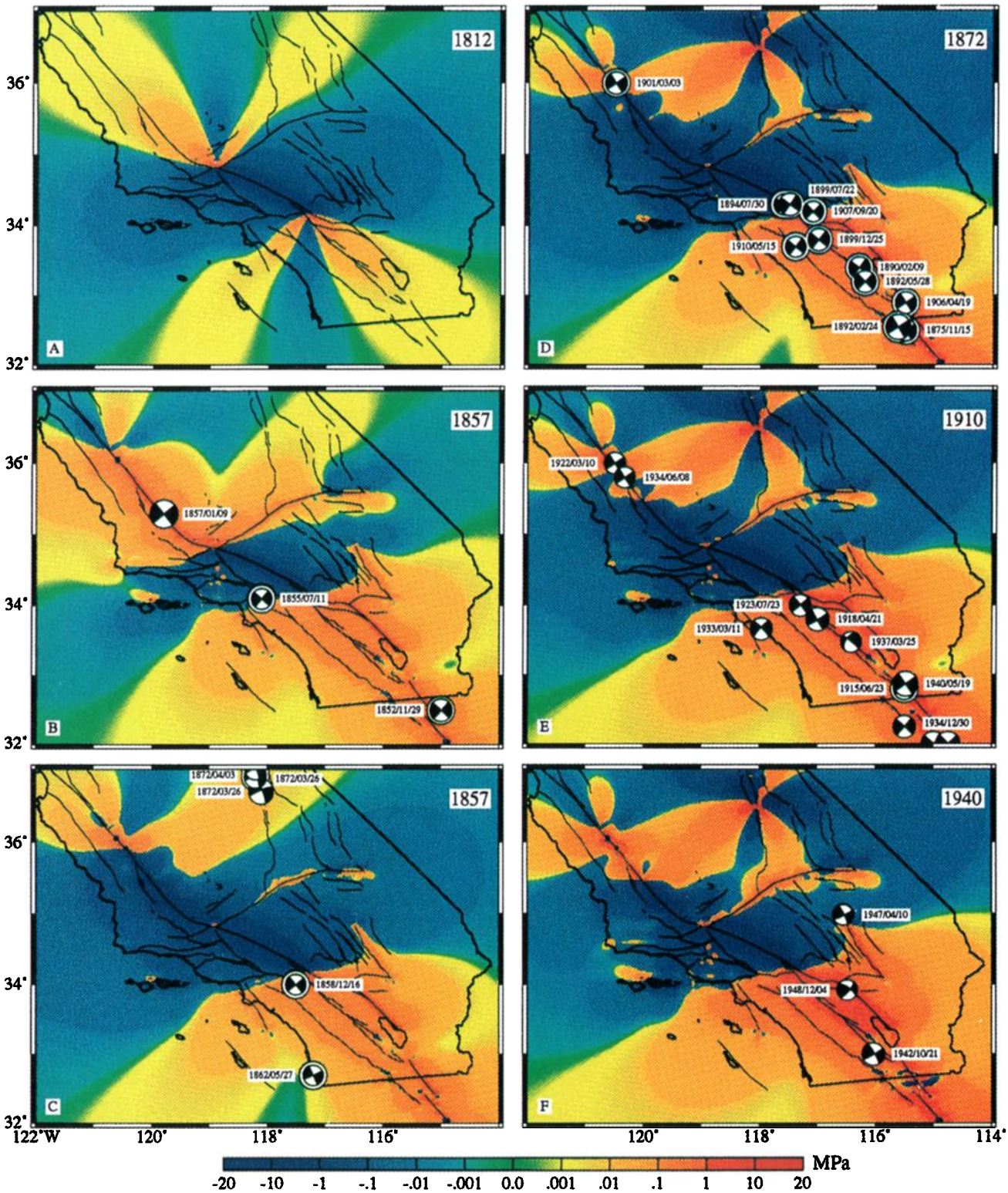

Plate 1. Stress evolution in southern California since great Wrightwood earthquake of 1812 on San Andreas fault. Coulomb stress is calculated for vertical planes striking 321°at depth of 8 km with changes denoted by color scale at bottom. The effective coefficient of friction μ is 0.6 for all diagrams. Coulomb failure function (ΔCFF) is taken to be zero everywhere before 1812 Wrightwood shock. Focal mechanism solutions for earthquakes larger than magnitude 6.0 with one nodal plane striking northwesterly and of steep dip are plotted on lower hemisphere equal-area projection. Earthquakes of different mechanisms are plotted separately in Plates 2 and 3. Black represents compressional first motion. Poorly known focal mechanism solutions are surrounded by a black and white loop. (a) Coseismic Coulomb stress changes associated with 1812 Wrightwood shock. (b) Stress evolution until just before great Fort Tejon earthquake of 1857. Focal mechanisms for events that occurred or are inferred to have occurred along NW trending strike-slip faults between 1812 and 1857 are plotted. (c) State of ΔCFF right after great Fort Tejon earthquake of 1857. Coseismic stress changes associated with the 1857 earthquake using the surface rupture model [*Sieh*, 1978] are included as well as evolution of stress changes since just before 1812 shock. Earthquakes that occurred between 1857 and 1872 included the Owens Valley sequence of 1872 (main shock and two aftershocks) are plotted. Note the stress shadow zone (dark blue colors) created by the great 1857 earthquake. (d) Right after the 1872 Owens Valley earthquake. Coseismic stress changes caused by the 1872 event are added to those in Plates 1a-1c. Focal mechanism solutions for earthquakes from 1872

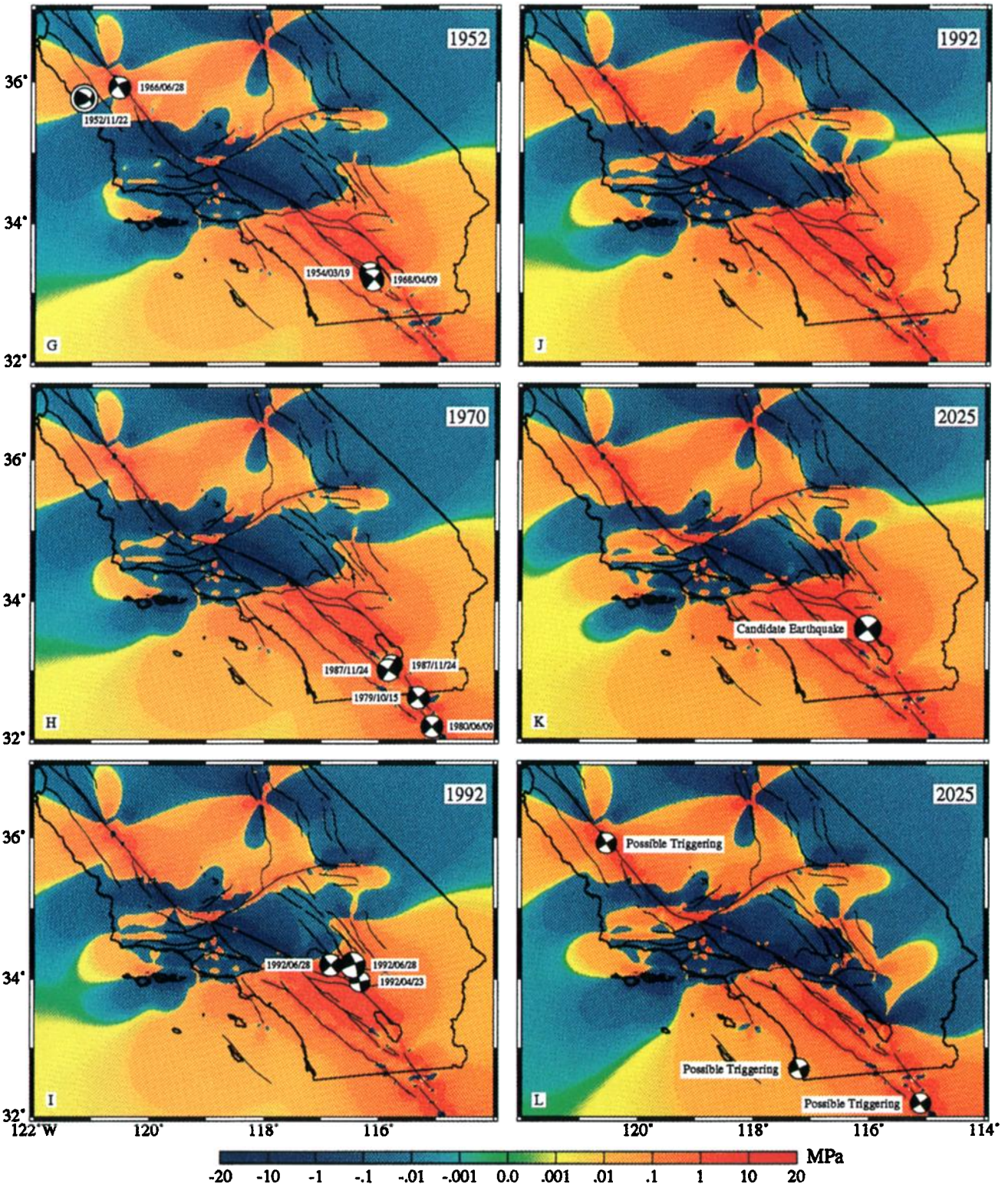

to 1910 are shown. Most of those events occurred in regions of positive ΔCFF. (e) Stress evolution until 1910 showing focal mechanism solutions for events between 1910 and 1940. (f) State of stress after 1940 Imperial Valley earthquake. Coseismic stress changes associated with the 1940 event are included in evolutionary model. Earthquakes between 1940 and 1952 are shown. Manix earthquake of 1947 actually occurred on a left-lateral NE trending fault, but stress model for that plane is similar to that calculated for right-lateral faulting of NW strike. (g) The ΔCFF just after 1952 Kern County earthquake. Events between its occurrence and 1970 are shown. (h) Stress evolution until 1970 showing earthquakes between 1970 and 1992. (i) The ΔCFF just before 1992 Landers earthquake. Focal mechanisms of the Landers earthquake sequence are plotted. (j) State of stress after 1992 Landers earthquake. (k) The ΔCFF in 2025 assuming no great shocks occur before that date. Mechanism shown is that of an assumed candidate great earthquake that ruptures both the San Bernardino and Coachella Valley segments of the San Andreas fault. Stress has increased greatly along these two segments since 1812. (l) Possible stress changes caused by the candidate great future earthquake are added into the evolutionary model. If this earthquake occurs, it is predicted to create a shadow zone of its own and move three regions of NW trending strike-slip faults closer to failure. Focal mechanism solutions are plotted for regions of positive changes in ΔCFF generated by candidate future earthquake where moderate-size events may be triggered. See *Deng and Sykes* [1996] for details of triggering by candidate future earthquake.

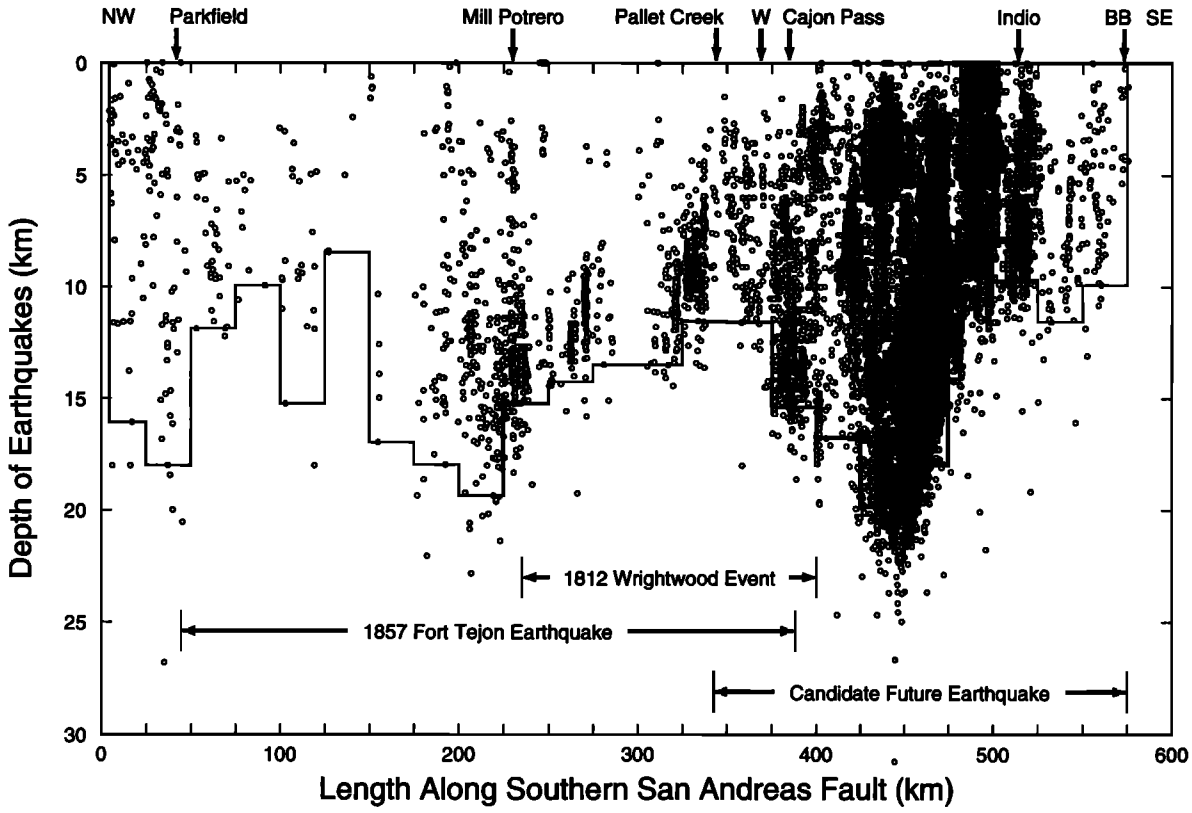

Figure 3. Cross section along southern San Andreas fault (thick line in Figure 1) showing projections of hypocentral locations of earthquakes that occurred within 10 km of the fault between 1981 and 1994 as determined by Southern California Seismographic Network (SCSN). Depths of deepest events vary considerably from less than 10 km to about 20 km along different segments. Thin lines show the depths above which 95% of earthquakes occurred along the corresponding segments. We use those depths to model the bottom of the seismogenic zone. Models of 1812 Wrightwood event, 1857 Fort Tejon earthquake, and a candidate future great earthquake are shown.

7.9 (Figures 3 and 4) are used in the evolutionary stress model. Their rupture characteristics are discussed in a later section.

The depths of the deepest earthquakes that occurred in southern California during the last 10 years vary from less than 10 to greater than 20 km [*Seeber and Armbruster*, 1995] (Figure 3). The bottom of the seismogenic zone is approximated to be that above which 95% of small, quality A earthquakes occurred from 1981 to 1994 as documented by the Southern California Seismographic Network (SCSN). Figure 3 shows the depth distribution of earthquakes close to the southern San Andreas fault.

Stress changes associated with both the virtual dislocations and actual earthquake displacements are calculated using a dislocation model of a planar fault surface Σ embedded in a homogeneous semi-infinite elastic medium, i.e., a half-space with zero tractions on the Earth's surface. *Steketee* [1958] showed that the displacement field u_k (kth component of u) in a semi-infinite elastic medium for an arbitrary uniform dislocation U across a surface Σ can be determined from

$$u_k = \frac{U_i}{8\pi\mu}\iint_{\Sigma} w_{ij}^{k} \nu_j \, d\Sigma \tag{1}$$

where μ is the shear modulus, ν_j are the direction cosines of the normal to the surface, U_i is the ith component of U, and w^k_{ij} are six sets of Green's functions.

The displacements and strain fields caused by finite rectangular sources are obtained by integrating (1) [*Okada*, 1992; G. Converse, U. S. Geological Survey, unpublished report, 1973]. The elastic stress s_{ij} is calculated from strain e_{ij} using Hooke's law for an isotropic medium

$$s_{ij} = \frac{2\mu\nu}{1-2\nu}\delta_{ij}e_{kk} + 2\mu e_{ij} \tag{2}$$

Here μ is shear modulus, ν is Poisson's ratio, and δ_{ij} is the Kronecker delta.

Earthquakes occur when the stress exceeds the strength of the fault. We quantify closeness to failure using the change in Coulomb failure function (ΔCFF) (modified from *Scholz* [1990]). It depends on both changes in shear stress $\Delta\tau$ and normal stress $\Delta\sigma$

$$\Delta CFF = \Delta\tau + \mu\Delta\sigma \tag{3}$$

Here μ is the apparent coefficient of friction. Both $\Delta\tau$ and $\Delta\sigma$ are calculated for a fault plane at the observing (field) point from the stress tensor described by (2). Change in shear stress $\Delta\tau$ is positive for increasing shear stress in the direction of relative slip on the observing fault; $\Delta\sigma$ is positive for increasing tensional normal stress. When compressional normal stress on a fault plane decreases, the static friction across the fault plane also decreases. Both positive $\Delta\tau$ and $\Delta\sigma$ move a fault toward failure; negative $\Delta\sigma$ and $\Delta\tau$ move it away from failure. A positive value

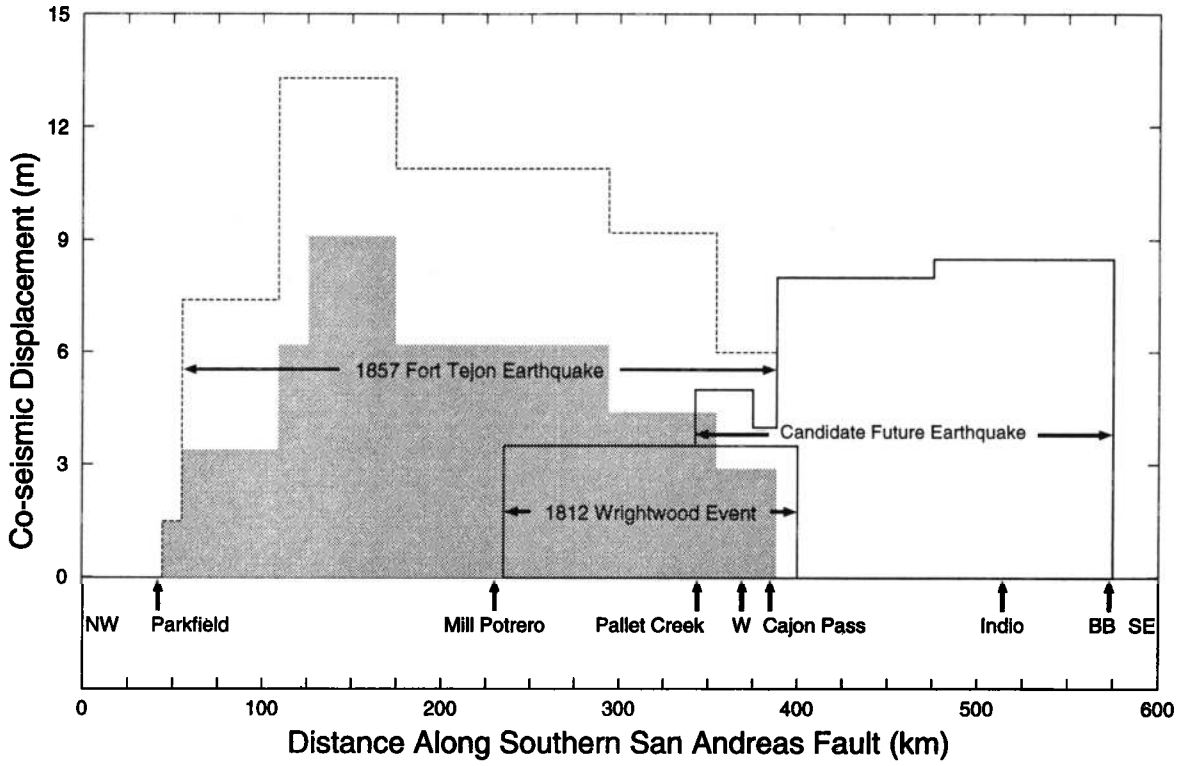

Figure 4. Coseismic displacement models for the 1812 Wrightwood earthquake, 1857 Fort Tejon earthquake, and candidate future great earthquake. The shaded region indicates the surface rupture model of *Sieh* [1978] for the 1857 event. The dashed line shows the slip deduced by *Pollitz and Sacks* [1992] for the same earthquake.

of ΔCFF for a particular fault denotes movement of that fault toward failure (that is, the likelihood that it will rupture in an earthquake is increased).

The apparent coefficient of friction μ is taken to be 0.2 or 0.6 throughout our calculations. Recent studies [e. g., *Rice,* 1992; *Miller et al.,* 1996] show that fluid pore pressures and their changes with time can be very important for active fault zones like the San Andreas fault. Low values of μ can result from either weak fault materials or high fluid pressures within active fault zones [*Hubbert and Rubey,* 1959]. The timescale for pore fluid to play a major role in changing the strength of fault zones after large or great earthquakes depends on the re-equilibration rate of fluids from regions adjacent to a fault segment or from deeper parts of the fault. That process is probably diffusive in character. That time constant is poorly known but probably ranges from several months to years [*Muir-Wood and King,* 1993]. When fluids are present, the term $\mu\Delta\sigma$ in (3) can be rewritten as $\mu'\Delta\sigma_{eff}$, where $\Delta\sigma_{eff} = \Delta\sigma + \Delta P$ and μ' is the actual coefficient of friction, $\Delta\sigma_{eff}$ is the change in effective (intergranular) normal stress, and P is the fluid pressure. If fluids are present in a fault zone at depth, a sudden change in $\Delta\sigma$ will lead to changes in both P and σ_{eff}. Thus the effective μ changes with time after great earthquakes. As the fluid pressure reequilibrates with time, σ_{eff} and the apparent coefficient of friction are also expected to change with time. The redistribution of fluid pressure may be very important on a timescale of months to years. Very little, however, is known about fluid diffusion at depth in active fault zones. Diffusivity is probably an anisotropic parameter, which may also vary with depth and with the long-term rate of fault movement. If fluid diffusion is, in fact, a very important effect, a low value of μ is predicted for the instantaneous behavior following a sudden change in normal stress, and a larger value would be appropriate once fluid diffusion is nearly completed. These are like undrained and drained conditions in soil and rock mechanics experiments. The two values of μ of 0.6 and 0.2 in this paper are end-member cases where fluid pressures are or are not restored.

A correlation between positive ΔCFF and faulting has been established for microearthquakes. *Reasenberg and Simpson* [1992] compared rates of microearthquakes in the 6 months after the 1989 Loma Prieta shock with those in the few years before its occurrence for a large number of nearby fault segments in the San Francisco Bay area. They found a good correlation between those changes and calculated values of ΔCFF for each segment using a dislocation model for slip in the 1989 earthquake. Their best correlation was obtained for a μ' of about 0.2. Consensus has not been reached, however, whether their low value of μ' should be attributed to high fluid pressures along fault zones in the bay area or to some other factor that leads to low steady state values of μ'.

We favor the hypothesis that significant fluid pressures are present at depth along major faults in California. Since we are mainly concerned in the evolution of ΔCFF on a timescale of decades, we present results mainly for the case of $\mu = 0.6$, assuming sudden changes in fluid pressure have had time to equilibrate. Nevertheless, we calculated changes for $\mu = 0.2$ and comment in the text when ΔCFF differs for the two cases.

Slip Rate Constraints

Long-term slip rates for major fault segments are constrained from paleoseismic, geologic, and geodetic measurements. *Petersen and Wesnousky* [1994] reviewed the first two kinds of

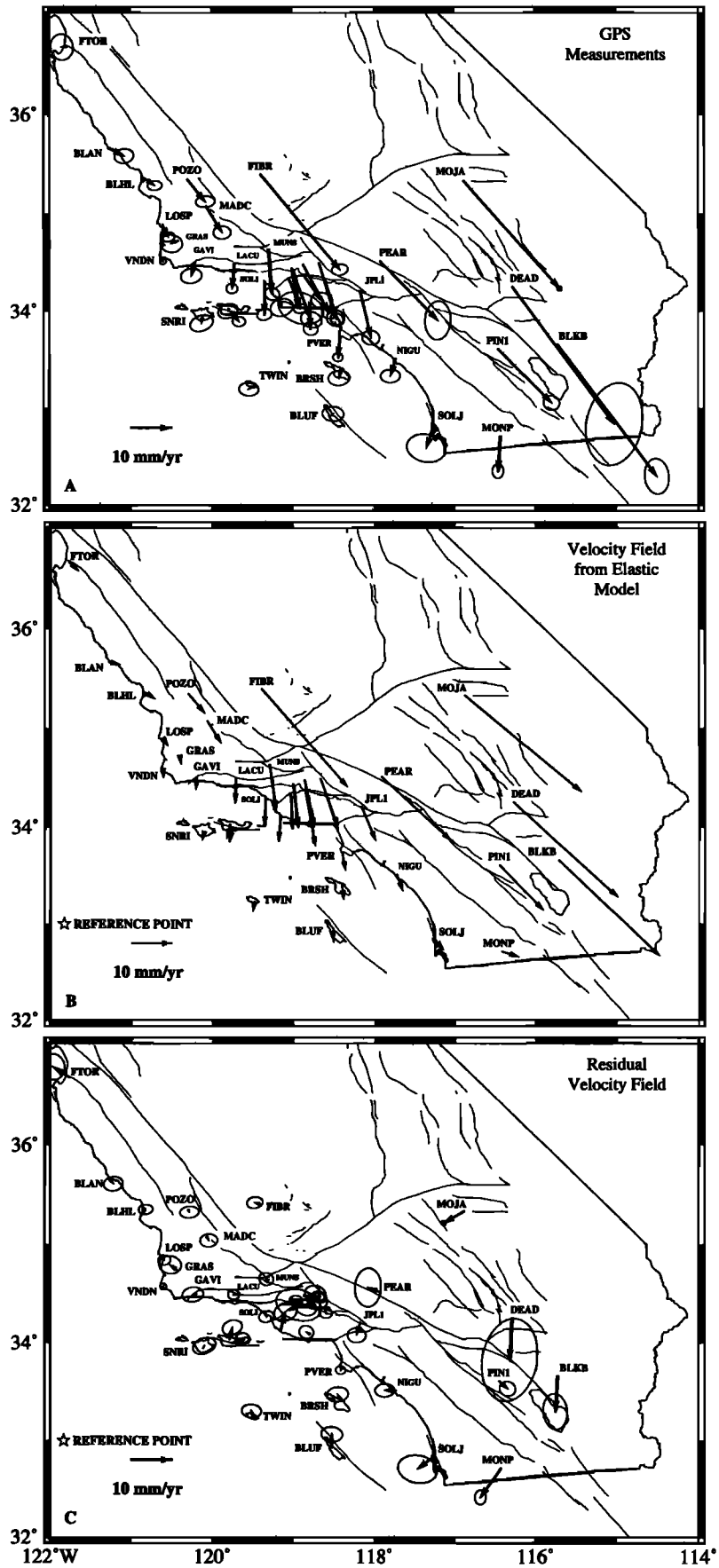
GPS
Measurements
10 mm/yr
A
Velocity Field
from Elastic
Model
☆ REFERENCE POINT
10 mm/yr
B
Residual
Velocity Field
☆ REFERENCE POINT
10 mm/yr
C
FTOR
BLAN
BLHL
POZO
FIBR
MADC
LOSP
GRAS
GAVI
VNDN
LACU
MUNS
SOLJ
SNRI
PVER
NIGU
TWIN
BRSH
BLUF
MOJA
PEAR
JPLJ
DEAD
FINI
BLKB
SOLJ
MONP
36°
34°
32°
122°W
120°
118°
116°
114°

measurements for a large number of faults in southern California. *Feigl et al.* [1993] summarized geodetic measurements for the 8 years prior to the 1992 Landers earthquake and calculated relative velocities for about 40 stations. Figure 5a shows the measurements obtained by *Feigl et al.* [1993]. The Pacific plate is taken to be rigid and fixed as a reference frame for the station velocities shown in Figure 5a. *Larson* [1993] determined the relative velocities for some offshore stations; the result is not significantly different from that of *Feigl et al.* [1993]. All geodetic and paleoseismic measurements together lead to first-order constraints on the slip rates of major faults in southern California.

Table 1 lists the 98 fault segments in southern California used in our calculations. The slip rates are mainly from *Petersen and Wesnousky* [1994], *Dolan et al.* [1995], and *Working Group on the Probabilities of Future Large Earthquakes in Southern California (Working Group)* [1995]. Most of the seismogenic depths of the strike-slip faults are determined from recent small earthquakes as described in the last section. For thrust faults or a few other strike-slip faults along which not enough small earthquakes occurred, the seismogenic depth is assumed to be 16 km.

Figure 5b shows the velocity field predicted by the half-space stress accumulation model using faults with long-term slip rates greater than 3 mm/yr. The fixed reference point is shown by the star in Figure 5b (bottom left). In our calculation those faults are taken to be locked from the surface to their seismogenic depths h. In addition to those 98 segments, two other semi-infinitely long segments are used: one extending northwesterly along the San Andreas fault from the central creeping segment to the northwest of Parkfield and the other southeasterly into Mexico from Cerro Prieto. With the 100 fault segments, about 75% of the tectonic loading along the plate boundary is included in our evolutionary model compared to the total relative motion between the Pacific and North American plates as determined from the NUVEL-1 model of *DeMets et al.* [1990]. The other 25% of the relative motion is more widely distributed in broad regions including eastern California, the Basin and Range area, and offshore regions.

Figure 5c shows the residual velocity field, i.e., the difference between data in Figures 5a and 5b, with the same reference point as in Figure 5b. Most of the residuals are within the 95% confidence ellipses, indicating that in most of southern California, the observed deformation pattern can be well modeled by our half-space model. Better constraints on rates can be obtained as more Global Positioning System (GPS) measurements become available. The residuals could be reduced somewhat by including (which we did not) the stress changes associated with the 1987 earthquake sequence near the southwestern end of the Salton Sea.

Several of the segments listed in Table 1 involve partial or total fault creep. In the model, only the seismic slip rate is used for stress accumulation. For example, the aseismic slip rate at Parkfield is about 12 while the whole slip rate is about 34 mm/yr [*Harris and Segall*, 1987]. The net effect is that of a fault with seismic slip rate of 22 mm/yr. No tectonic stress buildup associated with the fully creeping fault segment to the northwest of Parkfield is assumed. That segment is moving aseismically at a constant velocity in our model. However, its movement does not change whenever stress variation occurs on it as a result of stress buildup or earthquakes in other parts of California. That segment is not discussed further in the text.

Rupture Models for Large to Great Earthquakes

The coseismic displacements in the six largest earthquakes on land in southern California since 1812, i.e. those of $M_w \geq 7.0$ (Table 2), are included in our stress evolutionary model. Events of M_w near 7.0 that occurred offshore of southern California in 1812 and 1927 were not included in the stress modeling. Most of the rupture models discussed below are simplified and approximated by a number of rectangular patches with two edges parallel to the Earth's surface.

Wrightwood Earthquake of 1812

The first definitive evidence that the great 1812 Wrightwood earthquake occurred along the San Andreas fault came from dendrochronology. *Jacoby et al.* [1988] discovered that an earthquake in 1812 disturbed the annual ring width patterns of the trees growing along a 12-km segment of the San Andreas fault near Wrightwood, probably through changes in the distribution of groundwater in and near the fault zone. *Sieh et al.* [1989], *Fumal et al.* [1993], and K. Sieh (personal communication, 1995) indicate that the 1812 earthquake ruptured the San Andreas fault at trenching sites at Mill Potrero, Pallet Creek, Wrightwood, and Cajon Pass (Figures 1, 3, and 4).

Deng and Sykes [1996] calculated changes in stress in southern California associated with the 1812 Wrightwood earthquake on the San Andreas fault for two end-member rupture models. One is similar to that proposed by *Jacoby et al.* [1988], which is called the Wrightwood model. Another model is called the San Bernardino model, which we take to be less likely since rupture in 1812 appears to have occurred as far westward as Mill Potrero [*Sieh et al.*, 1989; K. Sieh, personal communication, 1995]. In the evolutionary model presented here, only the Wrightwood rupture model for the 1812 Wrightwood earthquake is used (Figures 3 and 4 and Table 3a). A displacement of 3.5 m for this segment [*Working Group*, 1995] is used extending from the Earth's surface to the seismogenic depth as shown in Figures 3 and 4. Since rupture may have been extended farther to the southeast in 1812, however, our estimate of $M_w = 7.5$ is probably a minimum. As shown in Figures 3 and 4, the event ruptured a segment of the San Andreas fault in which the seismogenic depth is shallower than that to the northwest of Mill Potrero or southeast of San Bernardino. This earthquake is not to be

Figure 5. (a) Global Positioning System (GPS) geodetic measurements as determined by *Feigl et al.* [1993]. Station velocities are with respect to a fixed Pacific plate. Ellipses indicate 95% confidence. (b) Velocity field predicted using elastic half-space model by locking the upper part of 100 fault segments including the 98 ones described in Table 1 and two semi-infinitely long segments, one extending northwest along San Andreas from central creeping section and the other extending southeast from Cerro Prieto fault. Reference point on Pacific plate is denoted by the star. (c) Residual velocity field determined by subtracting calculated field in Figure 5b from that observed in Figure 5a. Most residual velocities are within the 95% confidence level determined by *Feigl et al.* [1993] including those in the Transverse Ranges.

Table 1. Slip Rates for Major Fault Segments in Southern California

Segment Number	Name	Center		Strike, deg	Dip, deg	Length, km	Depth,* km	Fault Type†	Slip Rate, mm/yr
		Longitude, °W	Latitude, °N						
01	SACreeping1	120.681	36.112	138.5	90.0	20.6	0.0-16.1	RL	34‡
02	SACreeping2	120.531	35.980	136.0	90.0	19.3	0.0-18.0	RL	34§
03	SAParkfield1	120.433	35.895	139.1	90.0	6.5	0.0-18.0	RL	34§
04	SAParkfield2	120.331	35.787	143.6	90.0	23.9	0.0-11.9	RL	34‖
05	SACholame1	120.160	35.610	140.3	90.0	26.2	0.0-09.9	RL	34
06	SACholame2	119.985	35.434	141.8	90.0	24.2	0.0-15.2	RL	34
07	SACarrizo1	119.811	35.261	139.7	90.0	25.6	0.0-08.5	RL	34
08	SACarrizo2	119.627	35.100	133.9	90.0	23.6	0.0-17.0	RL	34
09	SACarrizo3	119.414	34.958	124.9	90.0	26.4	0.0-18.0	RL	34
10	SACarrizo4	119.163	34.860	105.4	90.0	25.1	0.0-19.4	RL	34
11	SACarrizo5	118.920	34.807	104.6	90.0	20.8	0.0-15.2	RL	34
12	SAMojave1	118.657	34.740	108.8	90.0	30.3	0.0-14.3	RL	30
13	SAMojave2	118.415	34.665	114.2	90.0	17.6	0.0-13.5	RL	30
14	SAMojave3	118.168	34.570	115.3	90.0	32.3	0.0-13.5	RL	30
15	SAMojave4	117.871	34.452	116.5	90.0	28.2	0.0-11.5	RL	30
16	SAMojave5	117.606	34.338	118.5	90.0	26.5	0.0-11.5	RL	30
17	SASanBernardino1	117.443	34.261	124.6	90.0	8.0	0.0-15.4	RL	24
18	SASanBernardino2	117.351	34.212	121.6	90.0	12.1	0.0-15.4	RL	24
19	SASanBernardino3	117.173	34.136	115.1	90.0	24.9	0.0-16.7	RL	24
20	SASanBernardino4	116.917	34.068	100.3	90.0	25.1	0.0-19.8	RL	24
21	SASanBernardino5	116.727	34.042	97.9	90.0	10.5	0.0-18.0	RL	24
22	SACoachella1	116.597	34.006	115.5	90.0	15.0	0.0-18.0	RL	25
23	SACoachella2	116.416	33.908	128.0	90.0	25.1	0.0-10.3	RL	25
24	SACoachella3	116.213	33.761	134.0	90.0	24.8	0.0-09.7	RL	25
25	SACoachella4	116.023	33.603	135.8	90.0	24.8	0.0-11.5	RL	25
26	SACoachella5	115.829	33.444	133.3	90.0	25.6	0.0-09.9	RL	25
27	SJSanBernardino2	117.450	34.209	128.7	90.0	13.3	0.0-15.2	RL	12
28	SJSanBernardino3	117.314	34.094	139.8	90.0	22.6	0.0-18.2	RL	12
29	SJSanJacinto1	117.227	34.008	138.6	90.0	2.4	0.0-18.2	RL	12
30	SJSanJacinto2	117.127	33.914	138.7	90.0	25.6	0.0-18.0	RL	12
31	SJSanJacinto3	116.976	33.785	130.9	90.0	14.4	0.0-18.8	RL	12
32	SJAnza1	116.871	33.715	125.4	90.0	10.6	0.0-18.8	RL	12
33	SJAnza2	116.715	33.621	126.1	90.0	25.1	0.0-18.5	RL	12
34	SJAnza3	116.499	33.488	126.8	90.0	24.7	0.0-16.8	RL	12
35	SJAnza4	116.259	33.344	124.8	90.0	30.2	0.0-13.4	RL	12
36	SJCoyoteCreek1	116.426	33.402	137.0	90.0	25.0	0.0-05.6	RL	4
37	SJCoyoteCreek1	116.277	33.267	137.5	90.0	15.8	0.0-12.2	RL	4
38	SJBorrego1	116.179	33.188	127.5	90.0	9.5	0.0-12.2	RL	4
39	SJBorrego2	116.057	33.087	137.7	90.0	22.5	0.0-11.6	RL	4
40	SJSuperstitionMountains	115.811	32.940	119.2	90.0	23.7	0.0-08.0	RL	4
41	SJSuperstitionHills	115.741	32.953	126.1	90.0	22.7	0.0-08.0	RL	4
42	ESWhittier	117.827	33.920	112.9	90.0	38.3	0.0-09.0	RL	3
43	ESGlenIvy1	117.568	33.835	137.8	90.0	11.4	0.0-09.0	RL	5
44	ESGlenIvy2	117.434	33.719	135.7	90.0	24.3	0.0-14.1	RL	5
45	ESTemecula1	117.241	33.564	132.1	90.0	25.3	0.0-15.3	RL	5
46	ESTemecula2	117.076	33.432	136.4	90.0	17.2	0.0-16.8	RL	5
47	ESJulian1	116.983	33.353	134.1	90.0	7.5	0.0-16.8	RL	5
48	ESJulian2	116.846	33.270	123.3	90.0	24.1	0.0-19.2	RL	5
49	ESJulian3	116.631	33.132	131.2	90.0	26.3	0.0-17.3	RL	5
50	ESJulian4	116.445	33.011	123.3	90.0	17.6	0.0-13.5	RL	5
51	ESCoyoteMountains1	116.320	32.956	106.4	90.0	9.1	0.0-13.5	RL	4
52	ESCoyoteMountains2	116.141	32.863	126.2	90.0	30.6	0.0-13.2	RL	4
53	IPImperial1	115.447	32.799	146.6	90.0	35.2	0.0-16.0	RL	30¶
54	IPImperial2	115.222	32.549	139.2	90.0	34.8	0.0-16.0	RL	30¶
55	IPCerroPrieto1	115.184	32.326	130.9	90.0	27.8	0.0-16.0	RL	30¶
56	IPCerroPrieto2	114.992	32.143	132.4	90.0	26.5	0.0-16.0	RL	30¶
57	IPCerroPrieto3	114.776	31.937	131.0	90.0	35.0	0.0-16.0	RL	30¶

Table 1. (continued)

Segment Number	Name	Center		Strike, deg	Dip, deg	Length, km	Depth,* km	Fault Type†	Slip Rate, mm/yr
		Longitude, °W	Latitude, °N						
58	LagunaSalada1	115.876	32.652	141.4	90.0	5.4	0.0-12.3	RL	4
59	LagunaSalada2	115.855	32.677	121.9	90.0	14.5	0.0-10.8	RL	4
60	LagunaSalada3	115.792	32.598	140.9	90.0	28.0	0.0-14.2	RL	4
61	LagunaSalada4	115.565	32.430	136.8	90.0	28.6	0.0-11.3	RL	4
62	LagunaSalada5	115.426	32.338	140.8	90.0	18.7	0.0-10.0	RL	4
63	Garlock1	118.581	34.956	66.4	90.0	27.5	0.0-13.0	LL	5
64	Garlock2	118.326	35.070	55.9	90.0	25.8	0.0-10.1	LL	5
65	Garlock3	118.103	35.204	51.4	90.0	24.4	0.0-10.0	LL	5
66	Garlock4	117.885	35.339	54.2	90.0	25.3	0.0-12.6	LL	5
67	Garlock5	117.639	35.448	68.4	90.0	26.0	0.0-11.7	LL	7
68	Garlock6	117.376	35.525	72.3	90.0	24.5	0.0-09.5	LL	7
69	Garlock7	117.108	35.582	78.3	90.0	25.6	0.0-11.9	LL	7
70	Garlock8	116.828	35.601	92.0	90.0	25.6	0.0-09.7	LL	7
71	Garlock9	116.510	35.600	89.0	90.0	32.0	0.0-06.0	LL	7
72	SMSanFernando	118.383	34.272	278.0	50.0	16.0	0.0-16.0	ST	4
73	SMAltadeno	118.157	34.208	295.1	55.0	28.5	0.0-16.0	ST	4
74	SMAsuza	117.839	34.145	273.3	55.0	32.6	0.0-16.0	ST	4
75	SMCucamonga	117.535	34.158	258.2	50.0	23.9	0.0-16.0	ST	5
76	PalosVerdes1	118.345	33.794	133.0	90.0	32.1	0.0-16.0	RL	3
77	PalosVerdes2	118.107	33.528	151.0	90.0	42.6	0.0-16.0	RL	3
78	SantaCruzIsland	119.702	34.014	98.9	90.0	53.2	0.0-16.0	LL	3
79	Pisgah	116.179	34.462	145.8	90.0	100.1	0.0-10.0	RL	5
80	VTRSanCayetano1	119.009	34.432	261.6	50.0	14.5	0.0-20.0	ST	5
81	VTRSanCayetano2	118.863	34.410	299.1	40.0	14.4	0.0-20.0	ST	8
82	VTRSantaSusana	118.624	34.340	276.7	60.0	32.5	0.0-16.0	ST	5
83	VTROakridge1	119.188	34.257	59.2	55.0	14.1	0.0-20.0	ST	5
84	VTROakridge2	119.064	34.318	59.0	55.0	12.6	0.0-20.0	ST	5
85	VTROakridge3	118.942	34.357	79.1	55.0	11.8	0.0-20.0	ST	5
86	VTROakridge4	118.835	34.367	90.0	55.0	8.2	0.0-20.0	ST	5
87	SMBTSantaMonica1	118.997	34.039	271.7	20.0	23.0	14.3-19.5	BT	4
88	SMBTSantaMonica2	118.749	34.029	273.9	20.0	22.7	14.3-19.5	BT	4
89	SMBTSantaMonica3	118.502	34.049	255.3	20.0	23.6	14.3-19.5	BT	4
90	SMBTSantaMonica4	118.259	34.092	261.1	20.0	22.3	14.3-19.5	BT	4
91	SMBTSantaMonica5	119.536	34.042	270.0	20.0	76.3	14.3-19.5	BT	4
92	Brawley	115.639	33.148	161.0	90.0	51.0	0.0-08.3	RL	25**
93	SCBTSanCayetano	119.500	34.500	270.0	20.0	183.3	14.3-19.5	BT	5
94	SMLLSantaMonica1	118.997	34.039	271.7	90.0	23.0	0.0-16.0	LL	3
95	SMLLSantaMonica2	118.749	34.029	273.9	90.0	22.7	0.0-16.0	LL	3
96	SMLLSantaMonica3	118.502	34.049	255.3	90.0	23.6	0.0-16.0	LL	3
97	SMLLSantaMonica4	118.259	34.092	261.1	90.0	22.3	0.0-16.0	LL	3
98	SMLLSantaMonica5	119.269	34.010	255.1	90.0	28.1	0.0-16.0	LL	3

Abbreviations are SA, San Andreas; SJ, San Jacinto; ES, Elsinore; IP, Imperial; SM, Sierra Madre; VTR, Ventura; SMBT, Santa Monica Blind Thrust; SCBT, San Cayetano Blind Thrust; SMLL, Santa Monica Left Lateral.

*Depth includes upper and lower limits for locked part of fault segment.

†RL is right-lateral strike slip; LL is left-lateral strike slip; ST is surface breaking thrust; BT is blind thrust.

‡Aseismic slip is 23 mm/yr; coseismic slip is 11 mm/yr [*Poley et al.*, 1987].

§Aseismic slip is 12 mm/yr; coseismic slip is 22 mm/yr [*Poley et al.*, 1987].

‖Aseismic slip is 3 mm/yr; coseismic slip is 31 mm/yr [*Poley et al.*, 1987].

¶Aseismic slip is 5 mm/yr; coseismic slip is 25.0 mm/yr [*Cohn et al.*, 1982].

**Aseismic slip is 5 mm/yr; coseismic slip is 20.0 mm/yr [*Savage et al.*, 1974].

confused with the earthquake of M = 7.1 near Santa Barbara 13 days later, which is described by *Deng and Sykes* [1996].

Great Fort Tejon Earthquake of 1857

Sieh [1978] conducted extensive mapping of surface ruptures of the San Andreas fault associated with the 1857 Fort Tejon earthquake (Figures 3 and 4 and Table 3b). His results indicate a non-uniform displacement pattern along strike. The slip value in one segment differs significantly from that of another segment. *Pollitz and Sacks* [1992] used triangulation observations made at the turn of the century to invert for the slip distribution during the 1857 earthquake. Their inversions are based on postseismic displacement calculations using an elastic/viscoelastic coupling model. Their preferred slip model shows 3 to 4 more meters of additional displacement compared to the surface measurements of *Sieh* [1978]. In the stress evolutionary model we mainly use the surface rupture model of *Sieh* [1978] throughout our calculations

Table 2. Source Parameters of $M \geq 6$ Earthquakes in Southern California between 1812 and 1994

Origin			Epicenter		D,										Mechanism, deg					
Year	Date	Time, UT	Longitude, °W	Latitude, °N	km	LQ*	Location	M_s	m_b	M_w	M_L	M_I	M_o, 10^{18}N-m	Strike	Dip	Rake	Method†	Q‡	References§
1812	Dec. 08	1500	117.65	34.37	0.0	a	Wrightwood	—	—	—	—	7.5	—	295	90	180	ISR	B	1,2,3,4
1812	Dec. 21	1900	119.90	34.20	0.0	c	Santa Barbara Channel	—	—	—	—	7.1	—	280	26	57	IOE	C	1,4
1852	Nov. 29	2000	115.00	32.50	0.0	c	Volcano Lake, B. C.	—	—	—	—	6.5	—	312	88	179	IOE	C	1,4
1855	July 11	0415	118.10	34.10	0.0	c	Los Angeles region	—	—	—	—	6.0	—	310	90	180	IOE	D	1,4
1857	Jan. 09	0812	119.80	35.30	0.0	a	Great Fort Tejon Earthquake	—	—	7.9	—	8.2	900.0	321	90	180	ISR	B	1,4,5,6
1858	Dec. 16	1000	117.50	34.00	0.0	b	San Bernardino region	—	—	—	—	6.0	—	321	90	180	IOE	C	1,4
1862	May 27	2000	117.20	32.70	0.0	c	San Diego region	—	—	—	—	5.9	0.1‖	336	90	180	IOE	C	1,4
1872	March 26	1030	118.10	36.70	0.0	a	Owens Valley	—	—	7.8	—	7.3	500.0	340	80	-171	ISR	B	1,4,5,6,7
1872	March 26	1406	118.20	36.90	0.0	c	Owens Valley	—	—	—	—	6.5	—	340	80	-171	IOE	C	1,4
1872	April 03	1215	118.20	37.00	0.0	c	Owens Valley	—	—	—	—	6.1	—	340	80	-171	IOE	C	1,4
1875	Nov. 15	2230	115.50	32.50	0.0	d	Imperial Valley to Colorado River delta	—	—	—	—	6.2	—	327	90	180	IOE	C	1,4
1883	Sept. 05	1230	119.90	34.20	0.0	c	Santa Barbara Channel	—	—	—	—	6.0	—	—	—	—	—	X	1,4
1885	April 12	0405	120.65	36.57	0.0	c	Southern Diablo Range	—	—	—	—	6.5	1.3‖	132	25	101	IOE	C	1,4,8
1890	Feb. 09	1206	116.30	33.40	0.0	c	San Jacinto or Elsinore fault region(?)	—	—	6.8	—	6.3	15.0	305	90	180	IOE	C	1,4,5
1890	April 24	1136	121.60	36.90	0.0	a	Pajaro Gap	—	—	—	—	6.0	0.9‖	314	90	180	IOE	C	1,4
1892	Feb. 24	0720	115.63	32.55	0.0	b	Laguna Salada, B. C.	—	—	—	—	7.2	500.0	328	90	180	IOE	C	1,4,5
1892	May 28	1115	116.20	33.20	0.0	c	San Jacinto or Elsinore fault region(?)	—	—	—	—	6.3	—	315	90	180	IOE	C	1,4
1894	July 30	0512	117.60	34.30	0.0	c	Lytle Creek region	—	—	—	—	6.0	0.4‖	305	90	180	IOE	D	1,4
1897	June 20	2014	121.50	37.00	0.0	a	Gilroy	—	—	—	—	6.2	4.2‖	321	90	180	IOE	C	1,4
1899	July 22	2032	117.50	34.30	0.0	b	Lytle Creek region	—	—	—	—	6.5	4.0	305	90	180	IOE	C	1,4,5
1899	Dec. 25	1225	117.00	33.80	0.0	a	San Jacinto and Hemet	6.4	—	6.8	—	6.7	15.0	309	90	180	IOE	D	1,4,5,6
1901	March 03	0745	120.50	36.00	0.0	x	Parkfield	6.4	—	—	—	5.8	—	327	90	180	IOE	C	1
1906	April 19	0030	115.50	32.90	0.0	x	Imperial Valley	6.2	—	—	—	5.8	—	327	90	180	IOE	C	1
1907	Sept. 20	0154	117.10	34.20	0.0	x	San Bernardino region	—	—	—	—	6.0	≤0.1	317	90	180	IOE	C	1,5
1908	Nov. 04	0837	117.00	36.00	0.0	x	Death Valley region	—	—	—	—	6.5	—	—	—	—	—	X	1
1910	May 15	1547	117.40	33.70	0.0	x	Glen Ivy Hot Springs	—	—	—	—	6.0	≤0.1	308	90	180	IOE	C	1,5
1915	June 23	0359	115.50	32.80	0.0	x	Imperial Valley	—	—	—	—	6.3	0.2	327	90	180	IOE	C	1,5
1915	June 23	0456	115.50	32.80	0.0	x	Imperial Valley	—	—	—	—	6.3	0.2	327	90	180	IOE	C	1,5
1915	Nov. 21	0013	115.00	32.00	9.0	x	Volcano Lake, B. C.	—	—	6.6	—	7.1	9.1	312	88	179	BWI	A	1,9
1916	Oct. 23	0244	118.90	34.90	0.0	x	Tejon Pass region	—	—	—	—	6.0	<0.1	—	—	—	—	X	1,5
1916	Nov. 10	0911	117.00	36.00	0.0	x	South of Death Valley	—	—	—	5.5	6.1	—	—	—	—	—	X	1
1918	April 21	2232	117.00	33.80	7.0	B	San Jacinto fault	—	—	6.8	6.8	6.6	14.0	150	87	-176	BWI	A	1,10
1922	March 10	1121	120.50	36.00	0.0	x	Parkfield	6.3	—	—	—	6.3	—	327	90	180	ISR	B	1,11
1923	July 23	0730	117.30	34.00	12.0	A	San Bernardino region	—	—	6.3	6.3	6.0	2.6	320	85	180	BWI	A	1,10
1925	June 29	1442	119.80	34.30	0.0	x	Santa Barbara	—	—	—	—	6.3	20.0	280	26	57	IOE	B	1,5
1927	Nov. 04	1350	120.90	34.35	10.0	a	Southwest of Lompoc	7.0	—	6.6	—	6.2	10.0	340	66	95	BWI	A	1,12
1933	March 11	0154	117.97	33.66	13.0	A	Long Beach	—	—	6.4	6.4	6.2	5.0	315	80	-170	BWI	A	1,13,14,15
1934	June 08	0447	120.33	35.80	0.0	B	Parkfield	—	—	6.4	6.1	5.6	4.4	327	90	180	ISR	B	1,14,15,16,17
1934	Dec. 30	1352	115.50	32.25	10.0	D	Laguna Salada, B.C.	—	—	6.5	6.5	—	6.1	311	88	180	BWI	A	1,9,15
1934	Dec. 31	1845	114.75	32.00	12.0	D	Colorado River Delta	—	—	7.0	7.1	—	31.0	317	89	180	BWI	A	1,9,15
1937	March 25	1649	116.41	33.47	3.0	B	Buck Ridge	—	—	5.6	6.0	5.9	0.3	309	83	-136	BWI	A	1,15,18,19

Table 2. (continued)

Origin			Epicenter		D,				M_s	m_b	M_w	M_L	M_I	M_o,	Mechanism, deg					
Year	Date	Time, UT	Longitude, °W	Latitude, °N	km	LQ*	Location							10^{18}N-m	Strike	Dip	Rake	Method†	Q‡	References§
1940	May 19	0436	115.48	32.87	7.0	A	Imperial Valley		7.2	—	7.0	6.9	—	22.5	325	90	180	BWI	A	1,6,14,18,20
1942	Oct. 21	1622	116.03	32.97	7.0	B	Fish Creek Mountains		—	—	6.3	6.6	—	3.3	61	88	10	BWI	A	1,14,18,21
1946	March 15	1349	118.05	35.73	22.0	A	Walker Pass		—	—	—	6.0	6.1	1.0	346	45	-117	BWI	A	1,5,14,22
1947	April 10	1558	116.55	34.98	5.0	A	Manix		—	—	6.5	6.5	—	6.0	65	85	8	BWI	A	1,14,15,23
1948	Dec. 04	2343	116.48	33.92	12.0	A	Desert Hot Springs		—	—	6.2	6.3	—	2-3	305	65	169	PFM	B	1,5,24,25,26
1952	July 21	1152	119.02	35.00	16.0	A	Great Kern County		7.8	—	7.5	7.5	7.0	110.0	73	75	50	EDM	B	1,5,6,15,27
1952	July 21	1205	119.00	35.00	0.0	D	Kern County		—	—	6.3	6.4	—	3.0	—	—	—	—	X	1,5,6,15
1952	July 23	0038	118.58	35.37	0.0	A	Kern County		—	—	—	6.1	—	0.4	50	—	-90	PFM	B	1,5,15,28
1952	July 29	0703	118.85	35.38	0.0	A	Bakersfield		—	—	6.3	6.1	—	3.0	53	90	—	PFM	B	1,5,6,15,28
1952	Nov. 22	0746	121.15	35.77	10.0	B	Bryson		—	—	—	6.0	6.0	—	309	66	145	PFM	C	1,15,29
1954	March 19	0954	116.18	33.29	9.0	B	Arroyo Salada		—	—	6.1	6.4	6.2	1.9	307	85	175	BWI	A	1,14,15,18,21
1966	June 28	0426	120.53	35.92	18.6	B	Parkfield		6.4	5.8	6.4	5.6	5.7	4.4	327	90	-160	PFM	A	1,15,17,30,31,32
1968	April 09	0228	116.13	33.19	10.0	B	Borrego Mountain		6.8	—	6.7	6.5	6.3	12.1	311	78	179	BWI	A	1,14,33
1971	Feb. 09	1400	118.40	34.41	8.4	B	San Fernando		—	—	6.7	6.6	6.5	17.0	293	52	72	PFM	A	1,14,34,35
1979	Oct. 15	2316	115.32	32.61	12.3	B	Imperial Valley		—	—	6.4	6.4	6.0	5.8	323	90	180	BWI	A	1,14,15,36
1980	June 09	0328	115.08	32.19	5.0	D	Victoria, B. C.		—	—	6.4	6.1	—	4.8	318	90	180	BWI	A	1,15,36
1983	May 02	2342	120.26	36.25	9.5	C	Coalinga		6.5	6.2	6.2	6.3	—	2.7	132	25	101	BWI	A	1,15,37
1987	Nov. 24	0154	115.78	33.08	8.0	A	Elmore Ranch fault		6.2	5.7	6.2	6.2	—	2.3	217	79	4	BWI	A	1,14,15,38
1987	Nov. 24	1315	115.84	33.01	10.0	A	Superstition Hills fault		6.6	5.9	6.6	6.6	—	10.0	303	89	-180	BWI	A	1,14,15,38
1992	April 23	0450	116.32	33.96	12.4	A	Joshua Tree		6.3	5.6	6.1	6.1	—	2.1	171	89	-177	LWI	A	15,39
1992	June 28	1157	116.44	34.20	8.0	A	Landers		7.5	—	7.3	7.4	—	110.0	340	74	-176	SWI	A	15,40,41
1992	June 28	1505	116.83	34.20	5.3	C	Big Bear		6.6	6.0	6.5	6.4	—	6.8	48	88	2	LWI	A	15,39
1994	Jan. 17	1230	118.54	34.21	18.4	A	Northridge		—	—	6.7	6.7	—	14.0	128	33	106	BWI	A	15,42

Abbreviations are D, depth; LQ, location quality; M_s, surface wave magnitude; m_b, body wave magnitude; M_w, moment magnitude; M_L, local magnitude; M_I, intensity magnitude; M_o, scale moment; and Q, focal mechanism quality. For double events, focal mechanism of main event is used; moment is sum of all events.

*Location quality [*Toppozada et al.*, 1981; *Southern California Seismographic Network*, 1995] is defined as follows: a, epicentral uncertainty ≤ 25 km or fault rupture identified; c, epicentral uncertainty ≤ 100 km; b, epicentral uncertainty ≤ 50 km; d, epicenter not controlled; x, information not available; B, ±2 km horizontal distance, ± 5 km depth; A, ± 1 km horizontal distance, ± 2 km depth; D, >± 5 km horizontal distance; and C, ± 5 km horizontal distance, no depth restriction.

†Methods are defined as follows: ISR, infered from surface rupture; IOE, inferred from mechanisms of other earthquakes including those by Seeber and Armbruster [1995]; BWI, body waveform inversion; PFM, P wave first-motion solution; EDM, elastic dislocation model; LWI, long-period waveform inversion; and SWI, surface waveform inversion.

‡Abbreviations are: B, good mechanism solutions, calculated from P wave first-motion data, geodetic data, elastic modeling, or inferred from surface rupture; C, reasonable focal mechanism solutions mainly inferred from other earthquakes; D, focal mechanism solutions not well constrained, mainly inferred from other earthquakes; X, information not available; and A, excellent focal mechanism solutions, calculated from waveform modeling or P wave first-motion data.

§References are 1, *Ellsworth* [1990]; 2, *Jacoby et al.* [1988]; 3, *Sieh et al.* [1989]; 4, *Toppozada et al.* [1981]; 5, *Hanks et al.* [1975]; 6, *Hanks and Kanamori* [1979]; 7, *Beanland and Clark* [1994]; 8, *Toppozada et al.* [1990]; 9, *Doser* [1994]; 10, *Doser* [1992]; 11, *Bakun and McEvilly* [1984]; 12, *Helmberger et al.* [1992]; 13, *Hauksson and Gross* [1991]; 14, *Hutton and Jones* [1993]; 15, *Southern California Seismographic Network*; 16, *Bakun and McEvilly* [1979]; 17, *Segall and Du* [1993]; 18, *Doser* [1990b]; 19, *Sanders et al.* [1986]; 20, *Doser and Kanamori* [1986]; 21, *Bent and Helmberger* [1991]; 22, *Dollar and Helmberger* [1985]; 23, *Doser* [1990a]; 24, *Nicholson* [1987]; 25, *Nicholson* [1996]; 26, *Nicholson et al.* [1987]; 27, *Stein and Thatcher* [1981]; 28, *Bath and Richter* [1958]; 29, *Dehlinger and Bolt* [1987]; 30, *McEvilly* [1966]; 31, *Smith and Wyss* [1968]; 32, *Wu* [1968]; 33, *Petersen et al.* [1991]; 34, *Heaton* [1982]; 35, *Whitcomb et al.* [1973]; 36, *Silver and Masuda* [1985]; 37, *Choy* [1985]; 38, *Sipkin* [1989]; 39, *Dziewonski et al.* [1993]; 40, *Kanamori et al.* [1992]; 41, *Qu et al.* [1994]; 42, *Song et al.* [1995].

||Scale moment was estimated using $\log M_o = 1.97 \log A_{VI} - 1.67$, of *Hanks et al.* [1975]. Moment is in N-m; A_{VI} is area of intensity VI, in m^2.

Table 3a. Rupture Model for Wrightwood Earthquake on San Andreas Fault on December 8, 1812

Segment Number	Center		Strike, deg	Dip, deg	Length, km	Depth, km	Displacement,* m
	Longitude, °W	Latitude, °N					
1	118.840	34.793	109.0	90.0	14.7	15.2	3.5
2	118.633	34.734	109.3	90.0	25.2	14.3	3.5
3	118.377	34.652	114.3	90.0	25.1	13.5	3.5
4	118.129	34.558	115.4	90.0	24.9	13.5	3.5
5	117.890	34.458	116.2	90.0	24.6	11.5	3.5
6	117.645	34.361	117.9	90.0	24.9	11.6	3.5
7	117.412	34.243	122.4	90.0	25.3	15.4	3.5

*Data are for right-lateral component only; see *Working Group* [1995].

Table 3b. Rupture Model for Fort Tejon Earthquake on San Andreas Fault on January 9, 1857

Segment Number	Center		Strike, deg	Dip, deg	Length, km	Depth, km	Displacement*	
	Longitude, °W	Latitude, °N					SS, m	PS, m
01	120.433	35.895	139.1	90.0	6.5	18.0	1.5	1.5
02	120.393	35.860	136.2	90.0	4.2	11.9	1.5	1.5
03	120.311	35.769	145.0	90.0	20.9	11.9	3.4	7.4
04	120.156	35.606	140.2	90.0	25.0	9.9	3.4	7.4
05	120.039	35.490	141.8	90.0	8.2	15.2	3.4	7.4
06	119.955	35.403	141.8	90.0	16.6	15.2	6.2	13.3
07	119.809	35.259	139.6	90.0	25.0	8.5	9.1	13.3
08	119.627	35.100	133.9	90.0	23.6	17.0	9.1	13.3
09	119.414	34.958	124.9	90.0	26.4	18.0	6.2	10.9
10	119.163	34.860	105.4	90.0	25.1	19.4	6.2	10.9
11	118.897	34.801	104.8	90.0	25.2	15.2	6.2	10.9
12	118.633	34.735	109.3	90.0	25.2	14.3	6.2	10.9
13	118.415	34.665	114.2	90.0	17.6	13.5	6.2	10.9
14	118.168	34.570	115.3	90.0	32.3	13.5	4.4	9.2
15	117.871	34.452	116.5	90.0	28.2	11.5	4.4	9.2
16	117.630	34.350	117.9	90.0	21.4	11.5	2.9	6.0
17	117.467	34.273	123.2	90.0	13.2	15.4	2.9	6.0

*Data are for right-lateral component only. Abbreviations are SS, surface slip [from *Sieh*, 1978]; PS, slip as deduced by *Pollitz and Sacks* [1992].

Table 3c. Rupture Model for Owens Valley Earthquake on March 26, 1872

Segment Number	Center		Strike, deg	Dip, deg	Length, km	Depth, km	Displacement*	
	Longitude, °W	Latitude, °N					SS, m	DS, m
1	118.314	37.151	338.0	80.0	23.7	16.0	4.0	0.4
2	118.220	36.964	338.0	80.0	21.2	16.0	4.0	0.4
3	118.131	36.787	338.0	80.0	21.3	16.0	7.0	1.0
4	118.059	36.602	347.0	80.0	21.8	16.0	10.0	1.0

*Displacement includes strike slip (SS) and dip slip (DS), positive for slip on right-lateral SS and normal DS [from *Beanland and Clark*, 1994].

Table 3d. Rupture Model for Imperial Valley Earthquake on May 19, 1940

Segment Number	Center		Strike, deg	Dip, deg	Length, km	Depth, km	Displacement,* m
	Longitude, °W	Latitude, °N					
1	115.399	32.733	143.7	90.0	12.0	16.0	2.0
2	115.327	32.650	143.7	90.0	10.8	16.0	1.0
3	115.258	32.576	139.5	90.0	10.2	16.0	5.0

*Data are for right-lateral component [from *Trifunac*, 1972].

Table 3e. Rupture Model for Kern County Earthquake on July 21, 1952

Segment Number	Center		Strike, deg	Dip, deg	Length, km	Depth,* km	Displacement†	
	Longitude, °W	Latitude, °N					SS, m	DS, m
1	119.00	35.00	73	75	25	5.0-27.0	-2.0	-2.4
2	118.80	35.15	58	35	25	3.5-15.0	-2.0	-1.0
3	118.57	35.27	43	20	25	2.0-10.0	-1.0	-0.4

*Depth indicates upper and lower boundaries of rupture zone.

†Displacement includes strike slip (SS) and dip slip (DS), positive for slip on right-lateral SS and normal DS [from *Stein and Thatcher*, 1981].

Table 3f. Rupture Model for Landers Earthquake on June 28, 1992

Segment Number	Center		Strike, deg	Dip, deg	Length, km	Depth, km	Displacement,* m
	Longitude, °W	Latitude, °N					
1	116.658	34.637	135.2	90.0	21.2	15.0	1.8
2	116.515	34.474	152.1	90.0	23.9	15.0	2.7
3	116.443	34.283	174.6	90.0	21.4	15.0	1.8

*Data are for right-lateral displacement only [from *King et al.*, 1994; *Wald and Heaton*, 1994].

Table 3g. Rupture Model for Candidate Future Great Earthquake on Southern San Andreas Fault

Segment Number	Center		Strike, deg	Dip, deg	Length, deg	Depth, deg	Displacement,* m
	Longitude, °W	Latitude, °N					
01	117.790	34.415	114.6	90	10.7	11.5	5.0
02	117.630	34.350	117.9	90	21.4	11.5	5.0
03	117.467	34.273	123.2	90	13.2	15.4	4.0
04	117.351	34.212	121.6	90	12.1	15.4	8.0
05	117.173	34.136	115.1	90	24.9	16.7	8.0
06	116.917	34.068	100.3	90	25.1	19.8	8.0
07	116.653	34.013	108.2	90	25.2	18.0	8.0
08	116.416	33.908	128.0	90	25.1	10.3	8.5
09	116.213	33.761	134.0	90	24.8	9.7	8.5
10	116.023	33.603	135.8	90	24.8	11.5	8.5
11	115.829	33.444	133.3	90	25.6	9.9	8.5

*Displacement is strike slip, positive for right-lateral slip.

and consider the inverted model of *Pollitz and Sacks* [1992] as an alternative to see what differences in stress the two models produce. We obtain M_w 7.9 and 8.1 for the two cases.

Owens Valley Earthquake of 1872

A great earthquake of M_w = 7.8 ruptured the Owens Valley fault zone in 1872. Rupture in that earthquake involved both strike-slip and dip-slip displacements, with a ratio of about 7:1. *Beanland and Clark* [1994] summarized observations at about 40 sites along the fault zone. Four fault segments are used in our stress evolutionary model (Table 3c); in each segment average displacements for both strike-slip and dip-slip motion are used.

Imperial Valley Earthquake of 1940

The M_w = 7.0 1940 Imperial Valley earthquake is the smallest event that is included in our calculations. This earthquake, a multiple event, was modeled by *Doser and Kanamori* [1987] using records of the Pasadena strain meter and five point sources along a 87.5 km long segment of the Imperial fault. *Trifunac* [1972] also concluded that the 1940 Imperial Valley earthquake involved at least four separate subevents by studying the strong-motion accelerogram at El Centro, which was located about 10 km northwest of the epicenter. He also inferred a slip distribution pattern from the accelerogram. In this study the displacements are grouped into three segments with a uniform slip value for each segment (Table 3d).

Kern County Earthquake of 1952

The 1952 M_w = 7.5 earthquake in Kern County is the only earthquake with a significant thrust component that is included in the stress change calculations. The earthquake occurred along the complex White Wolf fault. *Stein and Thatcher* [1981] used a combination of geodetic, geologic, and seismic data to constrain the fault planes and displacements in that shock. They identified three fault traces, each with a different lower depth of rupture, slip, and dip that best fit available observations. Table 3e shows these three fault segments with strike-slip and thrust components

of displacement. The rupture pattern obtained by *Stein and Thatcher* [1981] is used to calculate the coseismic stress changes associated with the 1952 earthquake.

Landers Earthquake of 1992

The 1992 Landers earthquake was extensively studied by seismologists and geologists [e.g., *Jaumé and Sykes*, 1992; *Harris and Simpson*, 1992; *Kanamori et al.*, 1992; *King et al.*, 1994]. *Wald and Heaton* [1994] determined a source rupture model for this earthquake. *King et al.* [1994] averaged their rupture pattern into 5x5 kilometer patches in a study of earthquake triggering. Our slip model is simplified into three segments, each with uniform displacement (Table 3f).

Focal Mechanisms of Moderate to Large Earthquakes

Table 2 lists all available source parameters for $M \geq 6.0$ earthquakes and is based on the catalog of *Ellsworth* [1990]. Five different magnitude scales are listed. M_s and m_b are surface and body wave magnitudes, respectively. M_w represents moment magnitude, which can be calculated from the scalar seismic moment [*Hanks and Kanamori*, 1979]. M_L is local magnitude, originally defined by *Richter* [1935] for the torsion seismometer [*Anderson and Wood*, 1925]. M_I is intensity magnitude based on reported felt effects by local residents. M_I is important especially for preinstrumental earthquakes.

Toppozada et al. [1978] published a catalog for $M \geq 6.0$ California earthquakes that occurred between 1900 and 1931; it is based mainly on reported felt effects. *Toppozada et al.* [1981] collected information on reported effects from old newspapers for major earthquakes that occurred before 1900. *Agnew* [1991] pointed out that the catalog is probably not complete for preinstrumental earthquakes since the intensity information for older events greatly depends on population distribution, especially prior to about 1850. *Toppozada* [1995] indicates that before 1880 the record of earthquakes of M~6 probably is incomplete. We listed in Table 2 all of the known events of $M \geq 6$ since 1812. Completeness, while desirable, is not essential to our conclusions. The SCSN catalog is complete at least down to M_L 4.0 since 1932 when data from a local seismic network were routinely reported.

Source parameters for most instrumentally recorded earthquakes in Table 2 are taken from published special studies. Some large to great shocks, such as those of 1857 and 1872, produced significant primary surface rupture. Their mechanisms can be inferred from those observations. Focal mechanism solutions for many other old earthquakes are not available directly and are approximated by us using well-determined mechanisms of more recent smaller earthquakes, most of which were determined by L. Seeber and J. Armbruster (personal communication, 1995) using data from the SCSN. No mechanism solutions are assigned to those several earthquakes that occurred in regions of very complicated faulting. Since a large uncertainty exists for even the epicentral locations of most older earthquakes, their focal mechanism solutions are assigned lower quality compared with those obtained by waveform inversions or first-motion studies. We are more confident of the source parameters determined from seismograms. The poorer mechanisms are designated by different symbols in various figures.

Stress Evolution and Triggering of Moderate-Size Earthquakes

Stress changes, i.e., values of ΔCFF, are computed for typical strike-slip and thrust faults in southern California. In our model the cumulative stress change for every location in southern California is a result of the interaction between all of the 98 fault segments described in Table 1 and the rupture models of the large to great earthquakes listed in Tables 3a-3g. The shear modulus and Poisson's ratio are fixed as 33 GPa and 0.25, respectively. In Plates 1 and 2, ΔCFF is calculated individually for strike-slip faults of San Andreas trend and for thrust faults of easterly strike using the surface rupture model [*Sieh*, 1978] for the 1857 Fort Tejon earthquake. The apparent coefficient of friction is fixed as 0.6 for Plates 1 and 2. Plate 3 shows the effect of using instead either the slip model deduced by *Pollitz and Sacks* [1992] for the 1857 event or a lower apparent coefficient of friction μ. In the plates, pure green indicates no significant change. Blue regions denote negative changes in Coulomb stress and decreased likelihood of fault rupture. These regions are called stress shadows following the usage of *Harris and Simpson* [1993, 1996]. Yellow to red regions represent positive ΔCFF and increased likelihood of rupture. The positive regions are called stress bright zones.

Keep in mind that stress is a tensorial, not a scalar, quantity. Thus shadow zones and bright zones must be viewed in the context of specific styles of fault slip, i.e., similar strike, dip, and rake. A particular location could be situated in a shadow zone for NW trending strike-slip faults, while it could be located in a bright zone for thrust faults of a given strike and dip. We will show that in each stage of the stress evolution calculations, most of the $M \geq 6$ earthquakes in the subsequent few decades occurred in bright zones, not in shadow zones. To do this, we only show mechanisms of moderate-size shocks of a similar type for which the stress calculations are performed. Much poorer agreement is obtained, for example, if a variety of mechanisms are plotted in a scalar sense. Initial values of ΔCFF are assumed to be zero everywhere on every fault plane just before the Wrightwood earthquake of 1812.

The ΔCFF for NW-SE Trending Strike-Slip Faults

Plates 1a-1l are snapshots of ΔCFF at a depth of 8.0 km for vertical right-lateral strike-slip faults striking 321°. The depth chosen for our calculations is not very critical providing it is several kilometers above the locking depths h shown in Figure 2. The strike of 321° is similar to that of most right-lateral strike-slip faults; it is also close to the direction of the relative plate motion between the Pacific and North American plates. Changes in stress for other fault planes are discussed later. The changes in stress are presented for the whole area of southern California rather than for specific faults. Of course, faults of a specific type do not exist everywhere.

Wrightwood earthquake of 1812. Plate 1a shows the coseismic stress changes associated with the large to great Wrightwood earthquake. This earthquake created shadow zones that probably affected the occurrence of future events. Note that the locations of the 1992 Landers sequence of earthquakes are situated just after 1812 in the shadow zones created by the Wrightwood shock. The shadow zones narrow with time either as stress is accumulated or changes take place following the occurrence of large to great events since 1812.

Great Fort Tejon earthquake of 1857. A great earthquake of magnitude M_w about 7.9 to 8.1 occurred on the San Andreas fault in 1857. Plates 1b and 1c show the state of stress before and after this earthquake with respect to the 1812 baseline. The coseismic stress changes associated with the 1857 Fort Tejon earthquake are included in Plate 1c but not in Plate 1b. Note that much of the rupture zone of the 1857 event was located in a region of positive ΔCFF just prior to its occurrence (Plate 1b). The *Sieh* [1978] model is used for the displacement distribution for the 1857 earthquake. Focal mechanism solutions for three earthquakes including the 1857 shock are plotted in Plate 1b. In Plate 1c earthquakes that occurred after 1857 until the 1872 Owens Valley earthquake sequence are shown. The information on some older earthquakes, for example, the 1858 and 1862 events, comes mainly from felt reports. Large uncertainties exist for both the locations and focal mechanism solutions of those events. The poor mechanism solutions are identified by a loop surrounding the lower hemisphere equal-area projection of the first motion.

The 1857 earthquake created a large shadow zone [*Harris and Simpson,* 1996] and four bright zones (Plate 1c). Two of the bright zones extend along the San Andreas fault system from the rupture tips of the 1857 event. Two others are located off the San Andreas fault, one that includes the Owens Valley region and another in the Borderland region of the Pacific Ocean off southernmost California. The 1857 Fort Tejon earthquake increased the stress along the 1872 Owens Valley rupture zone to a value slightly higher than the pre-1812 level. We think that the 1872 earthquake sequence was advanced by the stresses generated by the 1857 event. The two other bright zones extending from the tips of the 1857 rupture have been active for faulting of the San Andreas trend from 1857 to the present.

Owens Valley earthquake of 1872. Plate 1d shows the accumulated Coulomb stress changes just after the 1872 Owens Valley earthquake. This earthquake had more effect on nearby faults in eastern California than in the more southerly part of the state. Thus it did not appreciably change the overall stress pattern shown in Plate 1c except in nearby areas. A large number of earthquakes occurred in two of the bright zones created by the 1857 Fort Tejon earthquake in the 40 years after 1872 (Plate 1d). As discussed earlier, focal mechanism solutions for most of these older earthquakes are poorly determined and hence are marked by a black and white loop. During that period, stresses in these two bright zones continued to increase as a result of stress accumulation. The 1901 Parkfield earthquake is one example of a number of earthquakes that occurred in the central California bright zone. Note, however, the stress drops in those individual Parkfield shocks of $M \sim 6.5$ were not included in our calculations nor were those of events of $6 \leq M < 7$ along the San Jacinto fault.

Stress evolution until 1910. No great or significant earthquakes occurred in 1910. The arbitrary snapshot shown in Plate 1e merely indicates the state of stress evolution until that time. One difference between pre- and post-1910 earthquakes of moderate size is that the focal mechanism solutions for most of them from 1910 to 1940 (Plate 1e) are well determined from waveform inversions or reports of surface rupture. Most of those earthquakes continued to occur in the two bright zones of Plate 1e, including two at Parkfield and several along the San Jacinto and Imperial faults. The stress history along the Newport-Inglewood fault and its relationship to the 1933 Long Beach earthquake are discussed in a later section on faults with low long-term slip rates.

Imperial Valley earthquake of 1940. The stress pattern after the 1940 earthquake of M_w 7.0 on the Imperial fault is shown in Plate 1f. Focal mechanisms for moderate-size earthquakes between 1940 and 1952 are illustrated. An interesting earthquake that occurred in this period is the 1947 Manix event. This is the only shock in the central Mojave block that is shown in Plate 1. It occurred along a left-lateral strike-slip fault trending NE-SW rather than a NW striking fault [*Richter,* 1958; *Doser,* 1990a]. It is still plotted in Plate 1f since the stress patterns are similar for both types of mechanisms. The 1947 Manix earthquake occurred at the edge of a bright zone in our Coulomb stress model. Another interesting event that occurred in the same period is the 1948 Desert Hot Springs earthquake. That event occurred along the Coachella Valley segment of the southern San Andreas fault, indicating the increase of stress on that segment. *Nicholson et al.* [1987] studied the 1948 earthquake and compared it with the nearby M = 5.9 North Palm Springs shock of 1986. Since faulting is multibranched in that area [*Seeber and Armbruster,* 1995], however, it is not clear whether that event actually occurred on the "main" strand of the San Andreas fault.

Kern County earthquake of 1952. The state of ΔCFF just after the 1952 Kern County earthquake is shown in Plate 1g. The 1952 shock did not appreciably affect faults of San Andreas type since its mechanism was quite different. Several moderate-size earthquakes between 1952 and 1970 of appropriate mechanisms are also plotted. The 1966 Parkfield earthquake and two events on the San Jacinto fault zone occurred in bright zones of the Coulomb stress. The M 6.1 Bryson earthquake of November 22, 1952, occurred 4 months after the Kern County event. The Bryson earthquake along the coast of California is probably a complicated event, but no special study of it is known to us. The only available focal mechanism determined for it was performed by *Dehlinger and Bolt* [1987] using first-motion data. The P axis of the focal mechanism as determined by *Dehlinger and Bolt* [1987] trends NNW, while for almost all other focal mechanisms in Plate 1 it trends NE or NNE. An alternative possibility is that another set of nodal planes can be chosen to fit the first-motion data. The focal mechanism for this earthquake shown in Plate 1g and Table 2 is based on our refitting of the two nodal planes. It is located in a region of positive ΔCFF for the newly assigned focal mechanism. A better focal mechanism solution will not be available, however, until a special study is made using waveform modeling and a comparison of mechanisms of other events along the coast of central California. A more reliable mechanism solution would also make it clear if the Kern County earthquake 4 months earlier triggered this moderate-size event.

Stress in 1970. Plate 1h shows a snapshot of ΔCFF for 1970 and moderate-size earthquakes between 1970 and 1992. All of the latter occurred in the southernmost part of the San Andreas system. The 1987 Superstition Hills earthquake sequence was studied by *Hudnut et al.* [1989] in the context of cross-fault triggering. The first event occurred on the left-lateral, NE trending Elmore Ranch fault, while the second, 12 hours later, ruptured the adjacent right-lateral Superstition Hills fault of NW strike. Without including the coseismic stress changes of moderate-size earthquakes in our stress model, it is still clear that both earthquakes occurred in a bright zone. This is a good example to illustrate the idea of earthquake triggering; triggering does not mean that the coseismic stress change associated with one earthquake is enough to generate another earthquake in an originally stress-free location. It means, of course, that the stress at the location of the second earthquake is already close enough

to failure that the first earthquake can "trigger" the second one by introducing a positive increase in ΔCFF to move it into the failure regime. As discussed in a previous section, the stress changes since 1812 on left-lateral faults like the Elmore Ranch fault are similar to those on nearby perpendicular right-lateral strike-slip faults.

Landers earthquake of 1992. States of stress before and after the 1992 Landers earthquake are shown in Plates 1i and 1j, respectively. Focal mechanism solutions for the larger events in the sequence are shown in Plate 1i. The 1992 Landers earthquake is another example of stress accumulation on a fault with low long-term slip rate, whose epicenter was moved much closer to failure, mainly as a result of stress accumulation associated with nearby more active faults like the San Andreas. By the origin time the epicenter of the 1992 event was situated in the southern San Andreas bright zone. This is discussed more in a later section. The level of the maximum drops in stress associated with the Landers earthquake generated by our simple model is about 2.5 MPa, which gives the lower limit of fault strength of the Landers rupture zone.

Calculations for 2025. The Coulomb stress evolutionary calculations have been continued until 2025 assuming a large to great shock does not occur before then (Plate 1k). We then introduced a candidate future earthquake of M_w about 7.9 with its mechanism plotted in Plate 1k. The rupture model for that candidate shock is shown in Figures 3 and 4 and Table 3g. Displacement is assumed to be the slip accumulated since the occurrence of the last great earthquake on each segment that ruptures. Both the San Bernardino and Coachella Valley segments of the fault are assumed to rupture in that earthquake. Stress has been accumulating along the Coachella Valley segment since about 1690 [*Working Group,* 1995] and possibly along part or all of the San Bernardino segment since then. We suspect that most of the latter segment did not rupture in 1812 since the seismogenic depth (Figure 3) in that area is particularly great [*Seeber and Armbruster,* 1995; *Magistrale and Sanders,* 1996]. If rupture had, in fact, occurred in the "hard to break" San Gorgonio Pass region in 1812, it seems reasonable that it would have ruptured the Indio paleoseismic site in the Coachella Valley, which it did not [*Sieh et al.,* 1989].

Plate 1l indicates the state of stress in 2025 after the occurrence of the candidate great earthquake. A great earthquake like this can change the distribution of ΔCFF and trigger or shut off moderate seismicity in various regions of southern California. The three strike-slip focal mechanism solutions in Plate 1l represent the possible triggering in three bright zones of stress created by the candidate earthquake. However, unlike the 1857 event, it would decrease ΔCFF for the San Jacinto and Elsinore faults (Plates 1k and 1l), so moderate-size earthquakes likely would be shut off for at least decades before the stress built back to the precandidate earthquake level. The candidate earthquake introduced is just one possible example illustrating future triggering; it does not mean that we predict this earthquake to occur in 2025, with that magnitude or exact rupture length.

The ΔCFF for Thrust Faults

The snapshots shown in Plate 2 are more event and mechanism oriented; that is, the series of thrust fault planes chosen to calculate the stress patterns are based on the focal mechanism solutions of moderate to large earthquakes of interest that have occurred already. In contrast, in Plate 1 all calculations were for fault planes of the same strike, dip, and rake. Changes in stress are also computed for a depth of 8 km.

Wrightwood earthquake of 1812. The *M* 7.1 Santa Barbara earthquake occurred in southern California 13 days after the great 1812 Wrightwood earthquake. Plate 2a shows the state of stress for the assumed fault plane of the Santa Barbara earthquake after the great shock on the San Andreas. The mechanism of the Santa Barbara earthquake is taken to be that of a more recent event in 1978 in the same area [*Corbett and Johnson,* 1982]. The strike, dip, and rake for the 1978 earthquake are 280°, 26°, and 57°, respectively. *Deng and Sykes* [1996] discuss the possible triggering of the Santa Barbara earthquake by the great 1812 Wrightwood shock on the San Andreas fault. The ΔCFF was positive at that site for that and other styles of faulting typically found in the Santa Barbara Channel.

Stress evolution until 1880. Plate 2b illustrates the state of ΔCFF for the same set of fault planes in Plate 2a. Three earthquakes are plotted in Plate 2b. One moderate-size shock occurred in the Santa Barbara region in 1925. We take the mechanism to involve thrust faulting with a left-lateral component. Both focal mechanisms for recent earthquakes and constraints from geodetic measurements [*Larsen et al.,* 1993] indicate that the typical movement on faults in the Santa Barbara Channel is mainly a combination of thrust and left-lateral strike-slip faulting. *Willis* [1925] concluded that the 1925 earthquake was located very close to Santa Barbara based on local seismograms. *Toppozada et al.* [1990] compared the intensity distribution of the 1885 event with that of the 1983 Coalinga earthquake. They determined that the 1885 earthquake occurred about 50 km NW of Coalinga and was located along the same thrust zone and not along the San Andreas fault. We take its mechanism to be similar to that of the 1983 Coalinga earthquake. The most recent earthquake plotted in Plate 2b is the 1927 Lompoc event. *Helmberger et al.* [1992] calculated the source parameters of this shock using teleseismic records. While the exact location of that event is uncertain, it is clear that it occurred offshore. All of the three earthquakes shown in Plate 2b occurred in bright zones of ΔCFF for the mechanisms we assigned to them.

Kern County earthquake of 1952. Plate 2c illustrates ΔCFF just before the 1952 Kern County earthquake. The mechanism shown is that of the segment with the greatest rupture as determined by *Stein and Thatcher* [1981] for the 1952 earthquake. It is a high angle, south dipping plane. The 1952 earthquake occurred in a region of high positive Coulomb stress. Note that the orientation of the observing faults of the stress pattern for Plate 2c is the same as that of the main rupture zone of the 1952 earthquake, which is significantly different from that of Plate 2b.

State of stress in 1970. The state of stress is calculated for faults similar to that ruptured in the 1971 San Fernando earthquake (Plate 2d). The 1971 shock occurred on a north dipping plane [e.g., *Whitcomb et al.,* 1973]. The stress pattern shown in Plate 2d for 1970 is similar to that for 1880 (Plate 2b) because similar observing fault planes are used. The 1971 earthquake occurred in a bright zone of stress evolution. Our model is probably deficient in not including enough buildup of northerly directed compression. Doing so would increase ΔCFF even more for the 1971 style of faulting.

Northridge earthquake of 1994. The 1994 Northridge event was located close to that of the 1971 San Fernando earthquake. While the focal mechanisms for the two earthquakes are very similar, the 1994 earthquake occurred on a south dipping plane while the 1971 event was on a north dipping fault. Plate 2e shows the state of stress in 1994 on a series of fault planes parallel to the one that ruptured in 1994. The 1994 earthquake

occurred in a major bright zone of Coulomb stress. The focal mechanism of the 1983 Coalinga earthquake is also shown in Plate 2e. It occurred in a region of small positive ΔCFF but close to the boundary of bright and shadow stress zones. The state of stress along the fault that ruptured in the Coalinga earthquake could have been modified by either the 1906 San Francisco earthquake or the nearby Parkfield shock of 1966, neither of which is included in our stress evolutionary model. Note that none of the events in Plates 2a-2e occurred in stress shadow zones.

Calculations for 2025. Plate 2f illustrates the state of stress in 2025 subject to the same restrictions as described earlier for the candidate great earthquake. The calculations shown are for thrust faults with a small component of left-lateral strike-slip motion. The bright zones represent possible sites of future events of similar mechanism in the central and western Transverse Ranges and the Los Angeles Basin.

Stress Evolution Based on Alternative Parameters

A lower apparent coefficient of friction ($\mu = 0.2$) is used in Plates 3a-3c to calculate ΔCFF for three time periods for faults of San Andreas type. Such a low μ is representative of either very permanently weak faults or ones that are very weak soon after a major earthquake before significant fluid diffusion occurs so as to restore fluid pressure. Pore pressure may well change with time after great earthquakes, at least along certain faults. This process can increase μ, the apparent coefficient of friction, from a low value to a relatively high value. The stress patterns corresponding to the lower μ are very similar to those obtained in Plate 1 using a higher value. From 1857 onward the lower-μ based calculations yield slightly larger shadow zones, while the overall stress pattern is mainly preserved. The main result is not changed in that most $M \geq 6$ earthquakes occurred in bright stress zones of positive ΔCFF. In fact, the regions where ΔCFF differs significantly for the two values of μ were not the sites of known moderate-size events. This strengthens our finding that events occur in bright zones and not in stress shadows, but it does not allow us to discriminate the value of μ.

The difference between the two available rupture models for the great 1857 earthquake is that the displacements determined by *Sieh* [1978] from offsets at the surface are several meters less than those obtained by *Pollitz and Sacks* [1992]. If the *Pollitz and Sacks* [1992] model is used for the calculation of the coseismic stress changes associated with the 1857 earthquake, the stress shadow understandably decreases more slowly with time. For their model, the regions of negative changes in stress are larger than those shown in Plates 1c-1l. Plates 3d and 3e show ΔCFF in 2025 just prior to the proposed candidate great earthquake using the *Pollitz and Sacks* [1992] model for the 1857 shock and $\mu = 0.2$ and 0.6, respectively. Indeed, by 2025 the stress shadows in Plates 3d and 3e are much larger than those in the corresponding snapshots using the surface rupture model. The *Pollitz and Sacks* [1992] result is more uncertain than that of *Sieh* [1978] since it depends upon data for a period of time after 1884 and uses an uncertain viscosity in deriving coseismic slip in 1857.

A number of active E-W trending left-lateral strike-slip faults exist in the Transverse Ranges. Plate 3f shows ΔCFF for faults of that type in 2025 just before the candidate great earthquake. Bright regions are found in the western and central Transverse Ranges and in parts of the Los Angeles Basin.

Our calculations show that about 95% of those well-located moderate- to large-size earthquakes, with either strike-slip or dip-slip mechanisms, can be positively identified to occur in regions predicted to be bright stress zones where ΔCFF > 0. Others occurred at edges between bright and shadow zones. None of the $M \geq 6$ earthquakes occurred in areas of large negative ΔCFF. This result indicates that the Coulomb stress model can strongly constrain the location and occurrence of moderate- to large-size earthquakes and provide additional guides to long-term earthquake prediction.

Other Earthquakes

Thus far, we have discussed ΔCFF for strike-slip and thrust faults. The few remaining moderate-size earthquakes not included in Plates 1-3 are either those for which a reasonable focal mechanism could not be determined or inferred or events that occurred along normal faults. Moderate- to large- size, normal-faulting earthquakes in California have occurred mainly in the Sierra Nevada. One example of such a normal faulting was the Walker Pass earthquake of 1946 [*Dollar and Helmberger*, 1985]. They can be modeled better if a component of tectonic extension is added to our model in that region.

Stress History for Slow Moving Faults

As stated earlier, we did not include tectonic stress accumulation for faults with long-term slip rates less than 3 mm/yr. Faults with slower long-term rates often are moved either closer to or farther away from failure during the cycle of stress build up and release along more active nearby faults. The history of ΔCFF is examined for two slow-moving fault zones, the Newport-Inglewood fault and the series of faults that ruptured in the 1992 Landers earthquake. Both are right-lateral strike-slip faults. These two are good examples of fault interactions in southern California; large parts of these two rupture zones were moved away from failure, i.e., into shadow zones as a result of the 1812 earthquake (Figures 6 and 7). Stress accumulation associated with other fast-moving faults, however, brought the stress back to positive values in the next several decades. This very likely advanced the occurrence of earthquakes on those slow-moving faults.

Newport-Inglewood fault. Figure 6 shows the state of cumulative ΔCFF along the Newport-Inglewood fault from 1812 to 1933 just before the Long Beach earthquake using the surface rupture model for the 1857 Fort Tejon earthquake and $\mu = 0.6$. The evolutionary stresses differ only slightly if the model by *Pollitz and Sacks* [1992] is used for the 1857 shock. The 1857 Fort Tejon shock produced positive ΔCFF along the southern part of the Newport-Inglewood fault and small negative changes in stress along its northern part for $\mu = 0.6$ (Figure 6). The 1812 shock caused only small changes in ΔCFF. If $\mu = 0.2$ is used, however, both the 1812 and 1857 events produced small negative changes in stress along the entire Newport-Inglewood fault. The dominant change in ΔCFF along the fault from 10 to 60 km in Figure 6 results from stress accumulation associated with faults of faster long-term slip rate, such as the nearby Elsinore and faults offshore, as well as the San Andreas fault. The state of stress until just before the 1933 earthquake increased to positive values between 0.2 and 0.5 MPa along most of what was to become its aftershock zone [*Hauksson and Gross*, 1991]. Since the long-term rate of the Newport-Inglewood fault is very slow, this amount of positive change in ΔCFF was likely very significant in advancing the time of occurrence of the 1933 Long Beach earthquake.

The ΔCFF for the northern part of the fault also increased nearly monotonically after 1857 as a result of stress accumulation

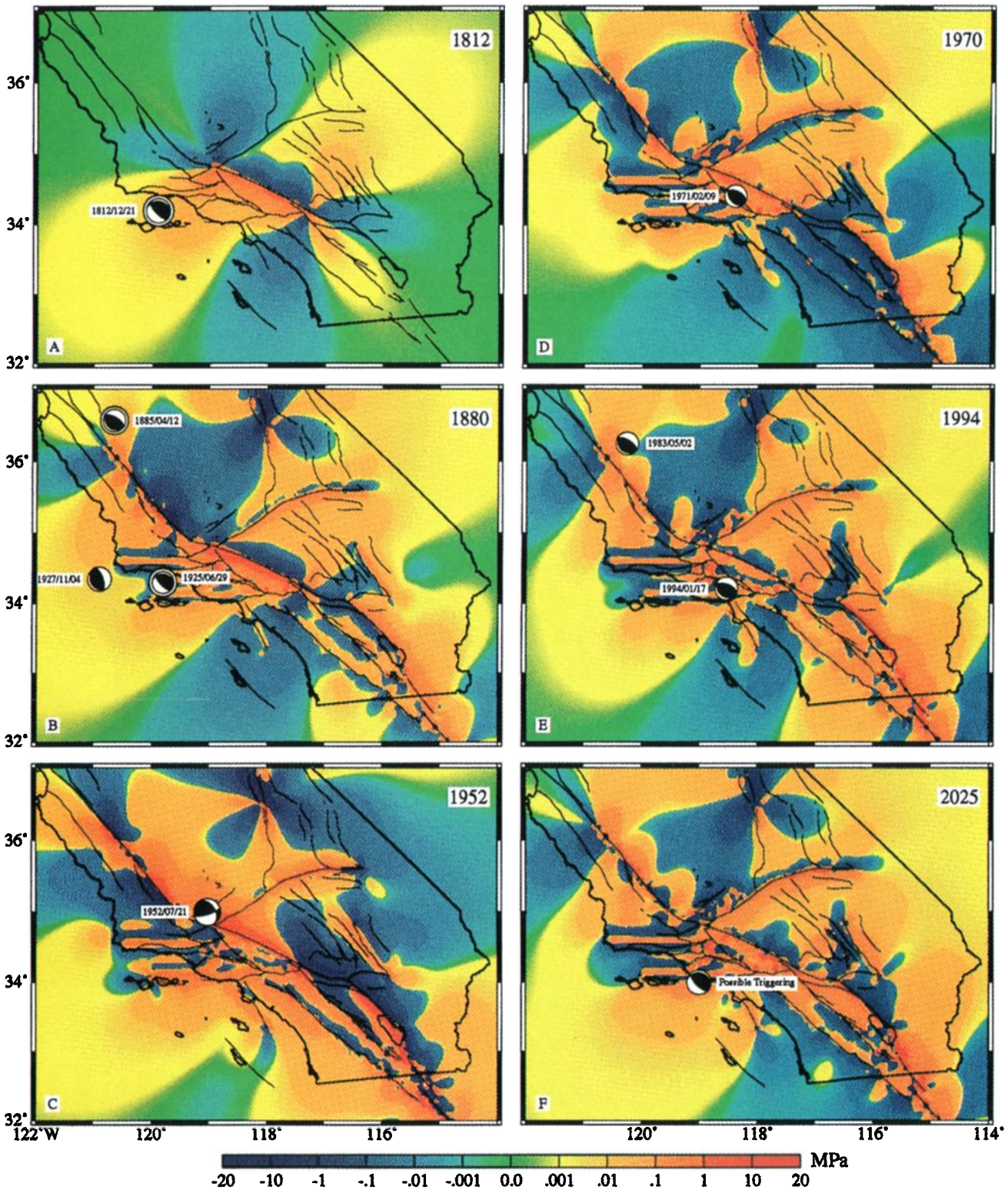

Plate 2. Coulomb stress evolution for various thrust faults calculated at depth of 8 km using effective coefficient of friction $\mu = 0.6$. E-W trending bands around Santa Barbara are generated by the several blind thrusts listed in Table 1. (a) Coseismic stress changes generated by great Wrightwood earthquake of 1812 on San Andreas fault for northerly dipping thrust faults of strike 280°, dip 26°, and rake 57°. The $M = 7.1$ Santa Barbara shock of 1812 may have been triggered by the great Wrightwood earthquake. (b) Stress evolution until 1880 for same set of fault planes as those in Plate 2a. Events from 1880 to 1927 of similar mechanism are shown. Location and inferred mechanism of 1885 earthquake are from *Toppozada et al.* [1990]. (c) State of ΔCFF just before 1952 Kern County earthquake for southerly dipping faults with strike 73°, dip 75° and rake 50°. The Kern Country earthquake occurred in a region of large positive ΔCFF. (d) Stress evolution until 1970 for northerly dipping faults with strike 293°, dip 52°, and rake 72°. San Fernando earthquake of 1971 occurred in a region of positive ΔCFF. (e) Evolution of the stress field until just before 1994 Northridge earthquake for southerly dipping faults of strike 128°, dip 33°, and rake 106°. Focal mechanism of 1983 Coalinga earthquake is also shown. (f) Stress evolution until 2025 for fault planes similar to those in Plate 2a. Possible changes in ΔCFF generated by future candidate great earthquake described in Plate 1k are added. If the candidate event occurs, calculations indicate that it will cause an increase in stress in several parts of western Transverse Ranges and Los Angeles Basin where stress has been building up during the last 200 years. Moderate to large earthquakes could be triggered as shown by focal mechanism.

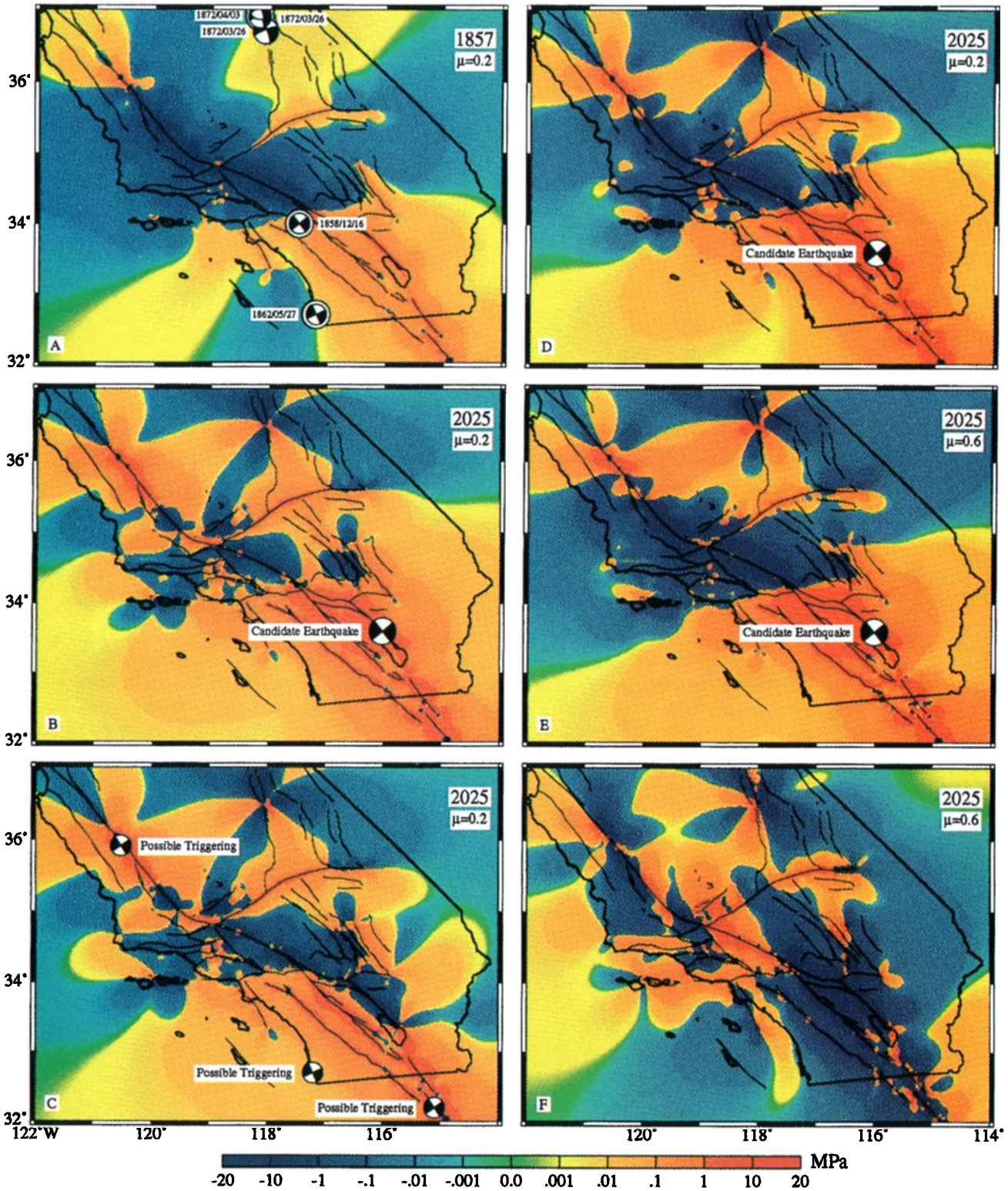

Plate 3. Coulomb stress evolution for various vertical strike-slip faults calculated at depth of 8.0 km showing the effects of different dislocation models associated with the great 1857 Fort Tejon earthquake, the effective coefficient of friction μ, and the fault strike. (a) Same as Plate 1c, (b) same as Plate 1k, and (c) same as Plate 1l (strike = 321°) except that μ = 0.2 is used instead of 0.6. (d) Same as Plate 3b, except that the slip model for great 1857 Fort Tejon event determined by *Pollitz and Sacks* [1992] (Table 3b) is used; Strike = 321°. (e) Same as Plate 3d, except μ = 0.6. (f) Same as Plate 1k, except that ΔCFF is calculated for E-W trending left-lateral strike-slip faults.

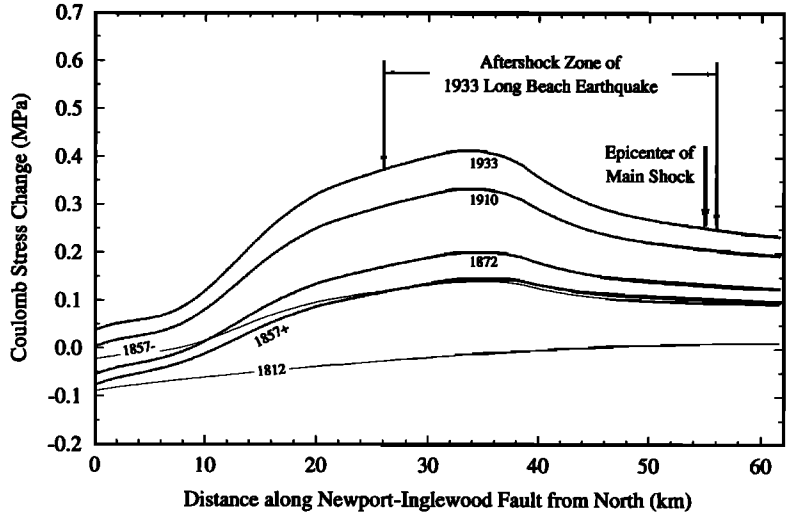

Figure 6. The ΔCFF along the Newport-Inglewood fault at depth of 8.0 km at several different times. The surface rupture model for the 1857 Fort Tejon earthquake and $\mu = 0.6$ are used. Here 1857^- (thin line) and 1857^+ (stippled line) represent the state of stress before and after the 1857 Fort Tejon event, respectively. Epicenter and aftershock zone of 1933 Long Beach earthquake are from *Hauksson and Gross* [1991].

associated with those faster-moving nearby faults. The 1933 event also loaded (not shown in Figure 6) the adjacent northern part of the fault that did not break in 1933. Since this part of the fault cuts through the metropolitan Los Angeles area, an earthquake of magnitude similar to that of the 1933 Long Beach event likely would be very destructive. Further study will be necessary to determine if this segment is close to rupture. Either an earthquake along that part of the Newport-Inglewood fault or a large event along either the Elsinore-Whittier or Palos Verdes faults could lower the present values of ΔCFF along the northern part of the Newport-Inglewood fault.

Landers rupture zone. Figure 7 shows the evolution of ΔCFF using the surface rupture model for the 1857 Fort Tejon earthquake and $\mu = 0.6$ for the series of faults that broke in the 1992 shock. The state of stress does not change much if we use the model of *Pollitz and Sacks* [1992] for the 1857 event or a lower μ value. The ΔCFF along large portions of the rupture zone of the 1992 Landers earthquake decreased 0.05-0.2 MPa during the 1812 and 1857 earthquakes. After 1857 the main feature of Figure 7 is large stress buildup near the southern end of the Landers rupture and smaller buildup at its northern end. Most of that increase results from rapid stress buildup along nearby parts of the San Andreas fault. Just before the 1992 shock, ΔCFF near its epicenter reached values as high as 0.5-0.8 MPa above the value before the occurrence of the great 1812 Wrightwood earthquake. Near the epicenter, stress was accumulating at a rate of about 0.4-0.5 MPa/century. That accumulated stress is expected to decrease when a large to great earthquake occurs on those nearby parts of the San Andreas fault. That decrease would be larger than what we computed for the 1812 and 1857 earthquakes.

The overall long-term interseismic stress field near a slow-moving fault is a combination of a very slow increase associated with buildup along that fault itself and one or more shorter periods of stress change associated with the cycle of stress buildup and release on neighboring fast-moving faults. Thus,

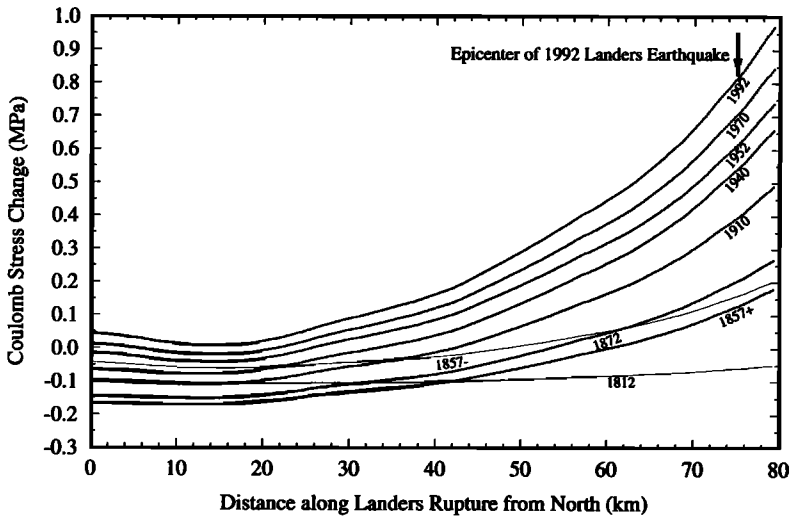

Figure 7. Same as Figure 6, except for ΔCFF along the 1992 Landers rupture zone.

during the relatively long cycle of Landers earthquakes, the stress field near its rupture zone is modulated by the occurrence of more frequent great earthquakes and subsequent stress buildup along the southern San Andreas fault. The high rate of stress increase since 1857 on the Landers rupture zone, especially near its epicenter, can probably answer the question raised by *Abercrombie and Mori* [1994]: why did the mainshock not rupture 13 years earlier following the Homestead Valley (M 5.2) earthquake of 1979 [*Hutton et al.*, 1980; *Stein and Lisowski*, 1983]? The 1979 shock occurred about 15 km north of the epicenter of the 1992 Landers event. The stress accumulation for NW-SE trending planes at the Landers epicenter from 1979 to 1992 is comparable to, not negligibly smaller than, the disturbance caused by the 1979 event. The 1979 shock mainly affected the region to the north of the 1992 epicenter. The occurrence of the 1992 Landers earthquake may also indicate that the state of stress along southern San Andreas fault has reached a level close to failure [*Jaumé and Sykes*, 1992].

State of Stress Along the Southern San Andreas Fault

The stress history for the southern San Andreas fault is shown in Figure 8 with ΔCFF=0 just before the 1812 earthquake. The calculations are done for a depth of 5 km. Stress at this depth is closer to the average value for corresponding seismogenic zones than that at 8 km. One important feature of Figure 8 is that the stress accumulation rate differs significantly from segment to segment along the southern San Andreas fault. The controlling parameter responsible for the variation in stressing is the seismogenic depth of each segment as shown in Figure 3 using recent seismicity. A deep seismogenic zone corresponds to a slow stress accumulation rate for a given rate of accumulation of potential displacement.

Most parts of the Mojave segment from Mill Potrero to Pallet Creek will continue to be in a stress shadow zone for at least several decades for the inverted slip model of *Pollitz and Sacks* [1992] for the 1857 Fort Tejon event (Figure 8b) but come closer to failure by 2025 for the surface rupture model (Figure 8a). These assessments depend critically, however, on the displacement and depth of faulting assumed for the 1857 earthquake. One or two segments between Parkfield and Mill Potrero are currently bright stress zones, depending upon the slip assumed for 1857. They are possible sites of moderate to large future earthquakes of $M \sim 7$. *Lienkaemper and Sturm* [1989] concluded that the surface rupture for the 1857 earthquake for the fault segment to the south of Cholame as determined by *Sieh* [1978] was underestimated. Their result for this segment is close to that of the slip model of *Pollitz and Sacks* [1992]. Thus ΔCFF shown in Figure 8b for their model should be a better approximation for that segment of the San Andreas fault. The ΔCFF for large part of the Carrizo Plain segment is still negative by 2025 in the two sets of calculations in Figure 8.

The stress along the Coachella Valley segment including Indio and BB in Figure 8 until 2025 ranges from 7 to 10 MPa. We assumed ΔCFF = 0 in 1812, whereas it may well have been strongly negative at that time as a result of a great shock about 1690. If we add loading since 1690, then the stress level along the Coachella Valley segment of the San Andreas fault is about 12 MPa until the present. However, the magnitude of ΔCFF along most parts of the San Bernardino and Coachella valley segments is still between 3 and 10 MPa higher than the level just before the 1812 earthquake. In addition, the 1992 Landers series moved parts of the San Bernardino segment of the San Andreas fault up to 0.4 to 0.8 MPa closer to failure [*Harris and Simpson*, 1992; *Jaumé and Sykes*, 1992; *Stein et al.*, 1992]. Thus a great earthquake rupturing both the San Bernardino and Coachella Valley segments could probably occur in the next few decades. Such an earthquake on the San Andreas fault could trigger earthquakes in other regions in southern California including the metropolitan Los Angeles area. *Deng and Sykes* [1996] describe the possible triggering as we mentioned earlier in discussing Plates 1-3.

Discussion

The coseismic displacements used in this study are all simplified to be uniform dislocation vectors across rectangular patches. The actual slip distribution in large and great earthquakes can be highly irregular. The complicated slip patterns and deviatoric regional stresses are probably responsible for the occurrence of aftershocks [King et al., 1994]. Our model does not mainly constrain the spatial distribution of aftershocks unless detailed and accurate coseismic slip patterns are available.

The ΔCFF pattern for NE-SW trending left-lateral strike-slip faults (for which we performed calculations but do not illustrate the results) is very similar to that of the NW-SE trending right-lateral strike-slip faults for which we show snapshots of the stress field. Thus Plate 1 also gives good indications of ΔCFF for faults of the Garlock type. In Plate 3f, as mentioned earlier, the state of stress is computed for E-W left-lateral strike-slip faults. Not as many earthquakes, of course, occur on left-lateral as on right-lateral faults in southern California.

Great earthquakes that occurred in northern California since 1812 could have affected the stress distribution on parts of the faults in this study. The 1906 San Francisco earthquake ruptured more than 400 km of the northern San Andreas fault [*Thatcher*, 1975]. That earthquake changed the stress distribution for faults in central [*Ben-Zion et al.*, 1993] and northern California [*Simpson and Reasenberg*, 1994; *Jaumé and Sykes*, 1996]. *Toppozada and Borchardt* [1996] recalculate a magnitude of about 7.5 for the 1838 earthquake along the San Francisco peninsular section of the San Andreas fault. They conclude that rupture in that event extended southeastward to San Juan Bautista in central California. The post-1838 patterns shown in Plates 1-3 may be slightly different for faults in central California if the stress changes caused by the 1906 and 1838 earthquakes and stress buildup associated with the northern San Andreas fault are included, as they were not in our study.

In our evolutionary stress model, only six $M \geq 7.0$ earthquakes and one candidate future great earthquake were used to calculate coseismic stress changes. Stress changes associated with the two $M \geq 7.0$ offshore earthquakes that occurred in 1812 and 1927 were not included. If the actual focal mechanism solutions of the two offshore earthquakes, in fact, involved mainly thrusting, then the stresses on thrust faults in the western Transverse Ranges and the Santa Barbara Channel will be slightly different from those shown in Plate 2. The stress model can also be improved at smaller wavelengths if good displacement models are used in the calculation for at least some earthquakes of $6<M<7$. Good estimates of displacements are available for several moderate-size shocks that occurred along the San Jacinto fault zone since 1890. Their use would provide better control on ΔCFF for much of the San Jacinto fault zone. Unknown or poorly known moderate-size shocks prior to about 1890 will always limit our knowledge of the state of stress. Probably several segments of faults that we show in the positive ΔCFF state are, in fact, not close to failure since they were the sites of previous moderate-size events for which information is lacking to model ΔCFF.

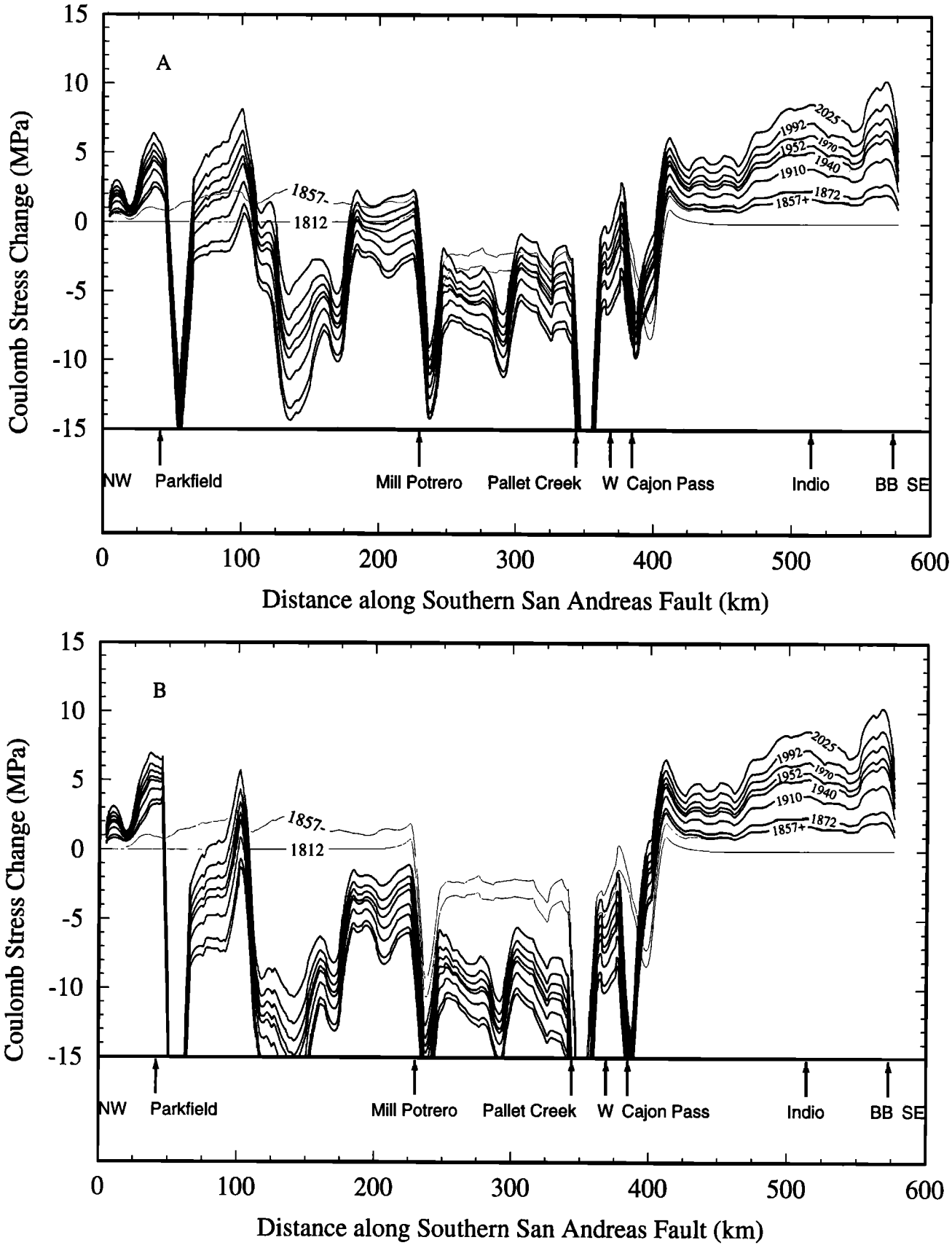

Figure 8. Same as Figure 7, except for ΔCFF along the southern San Andreas fault at depth of 5 km. Stress is smoothed to remove edge effects associated with individual fault patches. Apparent coefficient of friction $\mu = 0.6$. (a) Surface rupture model for the 1857 Fort Tejon earthquake. (b) Slip deduced by *Pollitz and Sacks* [1992] for the 1857 event.

One major assumption in the stress evolution calculations is that the strain rate for major faults in southern California is constant during the cycle of great earthquakes. Using a large number of geodetic measurements, *Savage and Lisowski* [1995*a*, *b*] discovered that the deformation rate along the San Andreas fault is steady at least for a timescale of about 20 years. Some authors have reported changes in rates of stressing following some great earthquakes [e.g., *Thatcher*, 1983]. Our models are deficient in that they are purely elastic and do not include time-dependent rheology, which probably is a significant factor, but on a debatable timescale.

The fact that about 95% of well located $M \geq 6$ earthquakes in southern California occurred in regions of positive ΔCFF indicates that the stress field can provide some guides to long-term earthquake prediction. The regions currently in large negative shadow zones are less likely sites of large to great earthquakes, while the areas in bright zones of high positive stress accumulation since 1812 are possible sites of future significant earthquakes if the stress is close enough to failure. The current ΔCFF (Plate 1) indicates that the Elsinore fault, the northern San Jacinto fault, and the Parkfield segment and the southern end of San Andreas fault are all in bright zones. We think that these are possible locations of moderate to large size strike-slip earthquakes during the next few decades.

Recent studies indicate that the rate of strain accumulation in the metropolitan Los Angeles area is greater than that released in earthquakes of the last 200 years [*Dolan et al.*, 1995; *Hough*, 1995]. Plates 2a-2f also show a long-term stress buildup in the same area. If a great earthquake ruptures the southern San Andreas fault, a sudden increase in the already positive stress field in the central and western Transverse Ranges and parts of the Los Angeles Basin could trigger moderate to large earthquakes much like the Santa Barbara shock of 1812 appears to have been triggered by the 1812 Wrightwood event on the San Andreas fault. Such earthquakes in populated parts of those areas could be very destructive [*Deng and Sykes*, 1996], much like the 1994 Northridge event was.

Our finding that so many $M \geq 6$ earthquakes in southern California since 1812 occurred in regions of calculated positive ΔCFF encourages us to continue our studies down to events of lower magnitude, like $M \geq 5$, using more realistic models [e.g., *Bird and Kong*, 1994] that take into account three-dimensional rheology as constrained by tomographic and other studies. In the future we plan to incorporate the stress drops of events of $6 < M < 7$ in our calculations. More work will be done to calculate the state of stress for slow-moving faults since about half of the large historic earthquakes in southern California occurred on faults of that type. Those with strongly positive values of ΔCFF with respect to our 1812 baseline, such as the northern end of the Newport-Inglewood fault, deserve greater scientific and social attention than those of strongly negative ΔCFF. GPS and other geodetic measurements can also be used to refine our stress accumulation models.

Conclusions

We constructed a model of the evolution of stresses in southern California for the period 1812-2025. Movement toward or away from failure is described in terms of the Coulomb failure function (ΔCFF). Tectonic stress loading is simulated by introducing negative virtual slip along the upper (locked) parts of major faults (i.e., those of long-term slip rates ≥ 3 mm/yr) as constrained from geologic and geodetic measurements. The unloading process is modeled by calculating coseismic stress changes associated with large to great earthquakes since 1812. All calculations were performed for an elastic semi-infinite half-space. Both high and low apparent coefficients of friction are used to bracket variations in pore pressure and fault strength. The model concentrates on the cumulative stress changes with time since just before a great earthquake on the San Andreas fault in 1812. Initial stresses just before the 1812 Wrightwood earthquake are assigned to be zero everywhere. Our calculations do not involve the absolute magnitudes of the components of the stress tensor since only changes in stress can be calculated with much precision.

We grouped our calculations as a series of snapshots in time for strike-slip and thrust faults. In southern California, where more than one style of active faulting occurs, it is necessary to model earthquake occurrence and stress changes in a tensorial rather than a scalar sense. For example, the 1952 Kern County shock had little effect on stresses associated with faulting of San Andreas strike, dip, and rake. Great earthquakes, such as those of 1812 and 1857, produced large shadow zones of negative ΔCFF, which gradually narrowed with time as stress was reaccumulated by tectonic loading. About 95% of those well-located $M \geq 6$ earthquakes can be identified to occur in bright zones, i.e., regions of positive ΔCFF. The ΔCFF for faults with slow long-term rates of displacement, such as those that ruptured in the 1933 Long Beach and 1992 Landers earthquakes, are modulated in time by stress accumulation and release associated with faster-moving faults. The epicenters of the 1933 and 1992 events had reached relatively high positive values of ΔCFF before their occurrence.

Our calculations indicate that the Coulomb stress model can strongly constrain the location of moderate- to large-size earthquakes. Maps of the current stress field can provide some additional guides to long-term earthquake prediction; that is, during the next few decades, earthquakes will likely occur in bright regions of ΔCFF. Along much of the San Bernardino and Coachella Valley segments of the San Andreas fault, ΔCFF is greater than 5 MPa with respect to our 1812 zero base level. Other major NW-SE trending right-lateral strike-slip faults with present positive values of ΔCFF include the northern San Jacinto fault and the Elsinore fault. Those fault segments are possible sites of large to great earthquakes during the next few decades. Large parts of the western and central Transverse Ranges are also bright zones for thrust faults and E-W trending left-lateral strike-slip faults. The stress pattern for NE-SW trending left-lateral strike-slip faults is similar to that of the NW-SE trending right-lateral strike-slip faults. Two long segments of the Garlock fault are sites of positive ΔCFF for such left-lateral strike-slip faults.

A candidate M 7.9 earthquake rupturing both the San Bernardino and Coachella Valley segments of the San Andreas fault is also introduced into our model for the year 2025. If this earthquake occurs, our calculations indicate that it will shut off moderate to large earthquakes along the northern San Jacinto and Elsinore faults but probably trigger earthquakes in three regions of strike-slip faults including Parkfield, the San Diego area, and the Imperial Valley. Thrust earthquakes of similar size could be triggered in several parts of the western and central Transverse Ranges including the Los Angeles metropolitan area. Our estimates for the appropriate timing and extent of rupture in a great earthquake along the southern San Andreas fault, however, are very much limited by uncertainties in the amount of displacement with depth for both the 1812 and 1857 great earthquakes and the extent of rupture along strike in 1812.

Acknowledgments. We thank R. Buck, R. Harris, Y. Kagan, W. Menke, C. Scholz, and T. Toppozada for critical reviews of the manuscript. L. Seeber and J. Armbruster gave us access to their unpublished catalog of focal mechanisms for more than 10,000 recent earthquakes in southern California. We thank D. Jackson and Y. Kagan for sending us their catalog of focal mechanism solutions for strong southern California earthquakes. We thank D. Agnew, J. Armbruster, J. Beavan, R. Buck, W. Ellswoth, K. Feigl, R. Harris, S. Jaumé, W. Menke, M. Petersen, J. Rice, C. Scholz, L. Seeber, K. Sieh, R. Simpson, X. Song, C. Sorlien, R. Stein, and T. Toppozada for discussion and comments. R. Harris sent us a preprint of her paper. We thank R. Simpson, who provided his dislocation program DLC1.1 using *Okada's* [1992] expressions. The stress field was calculated using DIS3D and checked with DLC1.1. DIS3D was originally written by S. Dunbar and later improved by *Erikson* [1986] using the expressions of G. Converse. We thank K. Hafner for giving us access to the SCSN data center. The GMT system [*Wessel and Smith*, 1991] was used to plot the color plates. This study was supported by NSF Cooperative Agreement EAR-8920136, USGS Cooperative Agreement 14-08-0001-A0899, and Southern California Earthquake Center grant number USCPO 569934 scope D. SCEC publication 339. Lamont-Doherty Earth Observatory contribution 5616.

References

Abercrombie, R., and J. Mori., Local observations of the onset of a large earthquake: 28 June 1992 Landers, California, *Bull. Seismol. Soc. Am., 84*, 725-734, 1994.

Agnew, D. C., How complete is the pre-instrumental record of earthquakes in southern California, in *Enviromental Perils San Diego Region*, edited by P. L. Abbott and W. J. Elliott, pp. 75-88, San Diego Association of Geologists, San Diego, 1991.

Anderson, J. A., and H. O. Wood, Description and theory of the torsion seismometer, *Bull. Seismol. Soc. Am., 15*, 1-72, 1925.

Bakun, W., and T. McEvilly, Earthquakes near Parkfield California: Comparing the 1934 and 1966 sequences, *Science, 205*, 1375-1377, 1979.

Bakun, W. H., and T. V. McEvilly, Recurrence models and Parkfield, California, Earthquakes, *J. Geophys. Res., 89*, 3051-3058, 1984.

Bath, M., and C. F. Richter, Mechanisms of the aftershocks of the Kern County, California, earthquake of 1952, *Bull. Seismol. Soc. Am., 48*, 133-146, 1958.

Beanland, S., and M. M. Clark, The Owens valley fault zone, eastern California, and surface faulting associated with the 1872 earthquake, *U. S. Geol. Surv. Bull., 1982*, 1-29, 1994.

Bent, A. L., and D. V. Helmberger, A re-examination of historic earthquakes in the San Jacinto fault zone, California, *Bull. Seismol. Soc. Am., 81*, 2289-2309, 1991.

Ben-Zion, Y., J. Rice, and R. Dmowska, Interaction of the San Andreas fault creeping segment with adjacent great rupture zones and earthquake recurrence at Parkfield, *J. Geophys. Res., 98*, 2135-2144, 1993.

Bird, P., and X. Kong, Computer simulations of California tectonics confirm very low strength of major faults, *Geol. Soc. Am. Bull., 106*, 159-174, 1994.

Choy, G. L., Source parameters of the Coalinga, California earthquake of May 2, 1983 inferred from broadband body waves, *U. S. Geol. Surv. Open File Rep., 85-44*, 83-103, 1985.

Cohn, S. N., C. R. Allen, R. Gilman, and N. R. Goulty, Preearthquake and postearthquake creep on the Imperial fault and the Brawley fault zone, *U. S. Geol. Surv. Prof. Pap., 1254*, 161-167, 1982.

Corbett, E. J., and C. E. Johnson, The Santa Barbara, California, earthquake of 13 August 1978, *Bull. Seismol. Soc. Am., 72*, 2201-2226, 1982.

Dehlinger, P., and B. A. Bolt, Earthquakes and associated tectonics in a part of coastal central California, *Bull. Seismol. Soc. Am., 77*, 2056-2073, 1987.

DeMets, C., R. G. Gorden, D. F. Argus, and S. Stein, Current plate motions, *Geophys. J. Int., 101*, 425-478, 1990.

Deng, J., and L. R. Sykes, Triggering of 1812 Santa Barbara earthquake by a great San Andreas shock: Implications of future seismic hazards in southern California, *Geophys. Res. Lett., 23*, 1155-1158, 1996.

Dolan, J. F., K. E. Sieh, T. K. Rockwell, R. S. Yeats, J. Shaw, J. Suppe, G. J. Huftile, and E. M. Gath, Prospects for larger or more frequent earthquakes in the Los Angeles metropolitan region, *Science, 267*, 199-205, 1995.

Dollar, R. S., and D. V. Helmberger, Body wave modeling using a master event for the sparsely recorded 1946 Walker Pass, California earthquake (abstract), *Eos Trans. AGU, 66*(46), 964, 1985.

Doser, D. I., A re-examination of the 1947 Manix, California, earthquake sequence and comparison to other sequences within the Mojave block, *Bull. Seismol. Soc. Am., 80*, 267-277, 1990a.

Doser, D. I., Source characteristics of earthquakes along the southern San Jacinto and Imperial fault zones (1937 to 1954), *Bull. Seismol. Soc. Am., 80*, 1099-1117, 1990b.

Doser, D. I., Historic earthquakes (1918 to 1923) and an assessment of source parameters along the San Jacinto fault system, *Bull. Seismol. Soc. Am., 82*, 1786-1801, 1992.

Doser, D. I., Contrasts between source parameters of M≥5.5 earthquakes in northern Baja California and southern California, *Geophys. J. Int., 116*, 605-617, 1994.

Doser, D. I., and H. Kanamori, Depth of seismicity in the Imperial Valley region (1977-1983) and its relationship to heat flow, crustal structure, and the October 15, 1979 earthquake, *J. Geophys. Res., 91*, 675-688, 1986.

Doser, D. I., and H. Kanamori, Long-period surface waves of four western United States earthquakes recorded by the Pasadena strainmeter, *Bull. Seismol. Soc. Am., 77*, 236-243, 1987.

Dziewonski, A. M., G. Ekstrom, and M. P. Salganik, Centroid-moment tensor solutions for April-June 1992, *Phys. Earth Planet. Inter., 77*, 151-163, 1993.

Ellsworth, W. L., Earthquake history, 1769-1989, *U. S. Geol. Surv. Prof. Pap., 1515*, 152-187, 1990.

Erikson, L., User's manual for DIS3D: A three-dimensional dislocation program with applications to faulting in the earth, M.S. thesis, 167 pp., Stanford Univ., Stanford, Calif., 1986.

Feigl, K. L., et al., Space geodetic measurement of crustal deformation in central and southern California, 1984-1992, *J. Geophys. Res., 98*, 21,677-21,712, 1993.

Fumal, T. E., S. K. Pezzopane, R. J. Weldon II, and D. P. Schwartz, A 100-year average recurrence interval for the San Andreas fault at Wrightwood, California, *Science, 259*, 199-203, 1993.

Hanks, T. C., and H. Kanamori, A moment magnitude scale, *J. Geophys. Res., 84*, 2348-2350, 1979.

Hanks, T. C., J. A. Hileman, and W. Thatcher, Seismic moments of the larger earthquakes of the southern California region, *Geol. Soc. Am. Bull., 86*, 1131-1139, 1975.

Harris, R. A., and P. Segall, Detection of a locked zone at depth on the Parkfield, California, segment of the San Andreas fault, *J. Geophys. Res., 92*, 7945-7962, 1987.

Harris, R. A., and R. W. Simpson, Changes in static stress on southern California faults after the 1992 Landers earthquake, *Nature, 360*, 251-254, 1992.

Harris, R. A., and R. W. Simpson, In the shadow of 1857, an evaluation of the stress changes generated by the M8 Ft. Tejon, California, earthquake (abstract), *Eos Trans. AGU, 74(43)*, Fall Meet. Suppl., 427, 1993.

Harris, R. A., and R. W. Simpson, In the shadow of 1857 - The effect of the great Ft. Tejon earthquake on subsequent earthquakes in southern California, *Geophys. Res. Lett., 23*, 229-232, 1996.

Harris, R. A., R. W. Simpson, and P. A. Reasenberg, Influence of static stress changes on earthquake locations in southern California, *Nature, 375*, 221-224, 1995.

Hauksson, E., and S. Gross, Source parameters of the 1933 Long Beach earthquake, *Bull. Seismol. Soc. Am., 81*, 81-98, 1991.

Heaton, T. H., The 1971 San Fernando earthquake: A double event?, *Bull. Seismol. Soc. Am., 72*, 2037-2062, 1982.

Helmberger, D. V., P. G. Somerville, and E. Garnero, The location and source parameters of the Lompoc, California, earthquake of 4 November 1927, *Bull. Seismol. Soc. Am., 82*, 1678-1709, 1992.

Hough, S., Earthquakes in the Los Angeles metropolitan region: A possible fractal distribution of rupture size, *Science, 267*, 211-213, 1995.

Hubbert, M. K., and W. W. Rubey, Role of fluid pressure in mechanics of overthrust faulting, I., mechanics of fluid-filled porous solids and its application to overthrust faulting, *Geol. Soc. Am. Bull., 70*, 115-166, 1959.

Hudnut, K. W., L. Seeber, and J. Pacheco, Cross-fault triggering in the November 1987 Superstition Hills earthquake sequence, southern California, *Geophys. Res. Lett., 16*, 199-202, 1989.

Hutton, L. K., and L. M. Jones, Local magnitudes and apparent variations in seismicity rates in southern California, *Bull. Seismol. Soc. Am., 83*, 313-329, 1993.

Hutton, L. K., C. E. Johnson., J. C. Pechmann, J. E. Ebel, J. W. Given, D. M. Cole, and P. T. German, Epicentral locations for the Homestead Valley earthquake sequence, March 15, 1979, *Calif. Geol., 33,* 110-114, 1980.

Jacoby, G. C., P. R. Sheppard, and K. E. Sieh, Irregular recurrence of large earthquakes along the San Andreas fault: Evidence from trees, *Science, 241,* 196-199, 1988.

Jaumé, S. C., and L. R. Sykes, Change in the state of stress on the southern San Andreas fault resulting from the California earthquake sequence of April to June 1992, *Science, 258,* 1325-1328, 1992.

Jaumé, S. C., and L. R. Sykes, Evolution of moderate seismicity in the San Francisco Bay region, 1850 to 1993: Seismicity changes related to the occurrence of large and great earthquakes, *J. Geophys. Res., 101,* 765-789, 1996.

Kanamori, H., H. K. Thio, D. Dreger, E. Hauksson, and T. Heaton, Initial investigation of the Landers, California, earthquake of 28 June 1992 using TERRAscope, *Geophys. Res. Lett., 19,* 2267-2270, 1992.

King, G. C. P., R. S. Stein, and J. Lin, Static stress changes and the triggering of earthquakes, *Bull. Seismol. Soc. Am., 84,* 935-953, 1994.

Larsen, S. C., D. C. Agnew, and B. H. Hager, Strain accumulation in the Santa Barbara Channel: 1970-1988, *J. Geophys. Res., 98,* 2119-2133, 1993.

Larson, K. M., Application of the Global Positioning System to crustal deformation measurements, 3, Result from the southern California borderlands, *J. Geophys. Res., 98,* 21,713-21,726, 1993.

Lienkaemper, J. J., and T. A. Sturm, Reconstruction of a channel offset in 1857 (?) by the San Andreas fault near Cholame, California, *Bull. Seismol. Soc. Am.*, 79, 901-909, 1989.

Magistrale, H., and C. Sanders, Evidence from precise earthquake hypocenters for segmentation of the San Andreas fault in San Gorgonio Pass, *J. Geophys. Res., 101,* 3031-3044, 1996.

Matsuura, M., D. D. Jackson, and A. Cheng, Dislocation model for aseismic crustal deformation at Hollister, California, *J. Geophys. Res., 91,* 12,661-12,674, 1986.

McEvilly, T. V., Preliminary seismic data, June-July 1966, *Bull. Seismol. Soc. Am., 56,* 967-971, 1966.

Miller, S. A., A. Nur, and D. L. Olgaard, Earthquakes as a coupled shear stress - High pore pressure dynamical system, *Geophys. Res. Lett., 23,* 197-200, 1996.

Muir-Wood, R., and G. C. P. King, Hydrological signatures of earthquake strain, *J. Geophys. Res., 98,* 22,035-22,068, 1993.

Nicholson, C., Slip on the southern San Andreas fault: 1948 and 1986 (abstract), *Seismol. Res. Lett., 58,* 14, 1987.

Nicholson, C., Seismic behavior of the southern San Andreas fault zone in the northern Coachella Valley, California: comparison of the 1948 and 1986 earthquake sequences, *Bull. Seismol. Soc. Am., 86,* 1331-1349, 1996.

Nicholson, C., H. Kanamori, and C. R. Allen, Comparison of the 1948 and 1986 earthquakes along the southern San Andreas fault, Coachella Valley, California (abstract), *Eos Trans. AGU, 68*(44), 1362, 1987.

Okada, Y., Internal deformation due to shear and tensile faults in a half-space, *Bull. Seismol. Soc. Am., 82,* 1018-1040, 1992.

Petersen, M. D., and S. G. Wesnousky, Fault slip rates and earthquake histories for active faults in southern California, *Bull. Seismol. Soc. Am., 84,* 1608-1649, 1994.

Petersen, M. D., L. Seeber, L. Sykes, J. Nabelek, J. Armbruster, and K. Hudnut, The interaction between secondary and master faults within the southern San Jacinto fault zone, southern California, *Tectonics, 10,* 1187-1203, 1991.

Poley, C. M., A. G. Lindh, W. H. Bakun, and S. S. Schulz, Temporal changes in microseismicity and creep near Parkfield, California, *Nature, 327,* 134-137, 1987.

Pollitz, F. F., and I. S. Sacks, Modeling of postseismic relaxation following the great 1857 earthquake, southern California, *Bull. Seismol. Soc. Am., 82,* 454-480, 1992.

Qu, J., T. L. Teng, and J. Wang, Modeling of short-period surface-wave propagation in southern California, *Bull. Seismol. Soc. Am., 84,* 596-612, 1994.

Reasenberg, P. A., and R. W. Simpson, Response of regional seismicity to the static stress change produced by the Loma Prieta earthquake, *Science, 255,* 1687-1690, 1992.

Rice, J. R., Fault stress states, pore pressure distributions, and the weakness of the San Andreas fault, in *Fault Mechanics and Transport Properties of Rocks; A festschrift in honor of W.F.Brace,* edited by Evans, B. and Wong, T.-F., pp. 475-503, Academic, San Diego, Calif., 1992.

Richter, C. F, An instrumental earthquake magnitude scale, *Bull. Seismol. Soc. Am., 25,* 1-32, 1935.

Richter, C. F., *Elementary Seismology,* pp. 516-518, W. H. Freeman, New York, 1958.

Sanders, C., H. Magistrale, and H. Kanamori, Rupture patterns and preshocks of large earthquakes in the southern San Jacinto fault zone, *Bull. Seismol. Soc. Am., 76,* 1187-1206, 1986.

Savage, J. C., A dislocation model of strain accumulation and release at a subduction zone, *J. Geophys. Res., 88,* 4984-4996, 1983.

Savage, J. C., and R. O. Burford, Geodetic determination of relative plate motion in central California, *J. Geophys. Res., 78,* 832-845, 1973.

Savage, J. C., and M. Lisowski, Geodetic monitoring of the southern San Andreas fault, California, 1980-1991, *J. Geophys. Res., 100,* 8185-8192, 1995a.

Savage, J. C., and M. Lisowski, Interseismic deformation along the San Anderas fault in southern California, *J. Geophys. Res., 100,* 12,703-12,717, 1995b.

Savage, J. C., D. D. Goodreau, and W. H. Prescott, Possible fault slip on the Brawley fault, Imperial valley, California, *Bull. Seismol. Soc. Am., 64,* 713-716, 1974.

Scholz, C. H., *The Mechanics of Earthquakes and Faulting,* Cambridge Univ. Press, New York, 1990.

SCSN, *Southern California Seismographic Network,* Pasadena, Calif., 1995.

Seeber, L., and J. G. Armbruster, The San Andreas fault system through the Transverse Ranges as illuminated by earthquakes, *J. Geophys. Res., 100,* 8285-8310, 1995.

Segall, P., and Y. Du, How similar were the 1934 and 1966 Parkfield earthquakes?, *J. Geophys. Res., 98,* 4527-4538, 1993.

Sieh, K. E., Slip along the San Andreas fault associated with the great 1857 earthquake, *Bull. Seismol. Soc. Am., 68,* 1421-1447, 1978.

Sieh, K., M. Stuiver, and D. Brillinger, A more precise chronology of earthquakes produced by the San Andreas fault in southern California, *J. Geophys. Res., 94,* 603-623, 1989.

Silver, P., and T. Masuda, A source extent analysis of the Imperial Valley earthquake of October 15, 1979, and the Victoria earthquake of June 9, 1980, *J. Geophys. Res., 90,* 7639-7651, 1985.

Simpson, R. W., and P. A. Reasenberg, Earthquake-induced static stress changes on central California faults, *U. S. Geol. Surv. Prof. Pap., 1550-F,* F55-F89, 1994.

Sipkin, S. A., Moment-tensor solutions for the 24 November 1987 Superstition hills, California, earthquakes, *Bull. Seismol. Soc. Am., 79,* 493-499, 1989.

Smith, S. W., and M. Wyss, Displacement on the San Andreas fault subsequent to the 1966 Parkfield earthquake, *Bull. Seismol. Soc. Am., 58,* 1955-1973, 1968.

Song, X., L. E. Jones, and D. V. Helmberger, Source characteristics of the 17 January 1994 Northridge, California, earthquake from regional broadband modeling, *Bull. Seismol. Soc. Am., 85,* 1591-1603, 1995.

Stein, R. S., and M. Lisowski, The 1979 Homestead Valley earthquake sequence, California: Control of aftershocks and postseismic deformation, *J. Geophys. Res., 88,* 6477-6490, 1983.

Stein, R. S., and W. Thatcher, Seismic and aseismic deformation associated with the 1952 Kern County, California, earthquake and relationship to the Quaternary history of the White Wolf fault, *J. Geophys. Res., 86,* 4913-4928, 1981.

Stein, R. S., G. C. P. King, and J. Lin, Change in failure stress on the southern San Andreas fault system caused by the 1992 magnitude=7.4 Landers earthquake, *Science, 258,* 1328-1332, 1992.

Stein, R. S., G. C. P. King, and J. Lin, Stress triggering of the 1994 M=6.7 Northridge, California, earthquake by its predecessors, *Science, 265,* 1432-1435, 1994.

Steketee, J. A., On Volterra's dislocations in a semi-infinite elastic medium, *Can. J. Phys., 36,* 192-205, 1958.

Thatcher, W., Strain accumulation and release mechanism of the 1906 San Francisco earthquake, *J. Geophys. Res., 80,* 4862-4872, 1975.

Thatcher, W., Nonlinear strain buildup and the earthquake cycle on the San Andreas fault, *J. Geophys. Res., 88,* 5893-5902, 1983.

Toppozada, T. R., History of damaging earthquakes in Los Angeles and surrounding area, in *The Northridge, California, Earthquake of 17 January 1994,* edited by M. C. Woods and W. R. Seiple, *Spec. Publ. 116,* pp. 9-16, Calif. Dep. of Conserv., Div. of Mines and Geol., Sacramento, 1995.

Toppozada, T. R., and G. Borchardt, Implications for the 1838 San Andreas fault earthquake, of relocating the 1836 earthquake to San Juan Bautista, *Eos Trans. AGU, 77(46),* Fall Meet. Suppl., F511, 1996.

Toppozada, T. R., D. L. Parke, and C. T. Higgins, Seismicity of California, 1900-1931, *Spec. Rep., Calif. Div. Mines Geol., 135,* 38 pp., 1978.

Toppozada, T. R., C. R. Real, and D. L. Parke, Preparation of isoseismal

maps and summaries of reported effects for pre-1900 California earthquakes, *Open File Rep. 81-11 SAC,* 182 pp., Calif. Div. of Mines and Geol., Sacramento, 1981.

Toppozada, T. R., C. Hallstrom, and D. Ransom, M ≥ 5.5 earthquakes within 100 km of Parkfield, CA., *Seismol. Res. Lett., 61*, 42, 1990.

Trifunac, M. D., Tectonic stress and the source mechanism of the Imperial Valley, California, earthquake of 1940, *Bull. Seismol. Soc. Am., 62,* 1283-1302, 1972.

Wald, D. J., and T. H. Heaton, Spatial and temporal distribution of slip for the 1992 Landers, California, earthquake, *Bull. Seismol. Soc. Am., 84,* 668-691, 1994.

Wald, D. J., H. Kanamori, D. V. Helmberger, and T. H. Heaton, Source study of the 1906 San Francisco earthquake, *Bull. Seismol. Soc. Am., 83,* 981-1019, 1993.

Wessel, P., and W. H. F. Smith, Free software helps map and display data, *Eos, Trans. AGU, 72,* 441, 445-446, 1991.

Whitcomb, J. H., C. R. Allen, J. D. Garmany, and J. A. Hileman, SanFernando earthquake series, 1971: Focal mechanisms and tectonics, *Rev. Geophys., 11,* 693-730, 1973.

Willis, B., A study of the Santa Barbara earthquake of June 29, 1925, *Bull. Seismol. Soc. Am., 15,* 255-278, 1925.

Working Group on the Probabilities of Future Large Earthquakes in Southern California, Seismic hazards in southern California: Probable earthquakes, 1994-2024, *Bull. Seismol. Soc. Am., 85,* 379-439, 1995.

Wu, F., Parkfield earthquake of June 28, 1966: Magnitude and source mechanism, *Bull. Seismol. Soc. Am., 58,* 689-709, 1968.

J. Deng and L. R. Sykes, Lamont-Doherty Earth Observatory, Columbia University, Palisades, NY 10964. (e-mail: jdeng@ldeo.columbia.edu; sykes@ldeo.columbia.edu)

(Received July 8, 1996; revised November 18, 1996;
accepted December 11, 1996.)